The Remnant of Supernova 1987A

Richard McCray[1] and Claes Fransson[2]

[1]Department of Astronomy, University of California, Berkeley, California 94720-3411; email: mccrayr@me.com

[2]Department of Astronomy, The Oskar Klein Centre, Stockholm University, Stockholm 10691, Sweden; email: claes@astro.su.se

Annu. Rev. Astron. Astrophys. 2016. 54:19–52

First published online as a Review in Advance on June 27, 2016

The *Annual Review of Astronomy and Astrophysics* is online at astro.annualreviews.org

This article's doi: 10.1146/annurev-astro-082615-105405

Keywords

supernovae, supernova remnants, nucleosynthesis, dust, molecules, shocks

Abstract

Although it has faded by a factor of $\sim 10^7$, SN 1987A is still bright enough to be observed in almost every band of the electromagnetic spectrum. Today, the bolometric luminosity of the debris is dominated by a far-infrared ($\sim$200 μm) continuum from $\sim$0.5 $M_\odot$ of dust grains in the interior debris. The dust is heated by UV, optical, and near-infrared (NIR) emission resulting from radioactive energy deposition by ^{44}Ti.

The optical light of the supernova debris is now dominated by illumination of the debris by X-rays resulting from the impact of the outer supernova envelope with an equatorial ring (ER) of gas that was expelled some 20,000 years before the supernova explosion. X-ray and optical observations trace a complex system of shocks resulting from this impact, whereas radio observations trace synchrotron radiation from relativistic electrons accelerated by these shocks. The luminosity of the remnant is dominated by an NIR ($\sim$20 μm) continuum from dust grains in the ER heated by collisions with ions in the X-ray emitting gas.

With the Atacama Large Millimeter Array (ALMA), we can observe the interior debris at millimeter/submillimeter wavelengths, which are not absorbed by the interior dust. The ALMA observations reveal bright emission lines from rotational transitions of CO and SiO lines that provide a new window into the interior structure of the supernova debris. Optical, NIR, and ALMA observations all indicate strongly asymmetric ejecta.

Intensive searches have failed to yield any evidence for the compact object expected to reside at the center of the remnant. The current upper limit to the luminosity of such an object is a few tens of solar luminosities.

Contents

1. INTRODUCTION 20
2. ENERGY SOURCES AND LIGHT CURVES 22
3. THE DEBRIS 26
   3.1. Optical/IR Emission 26
   3.2. Ejecta Structure 27
   3.3. Dust Formation 31
4. CIRCUMSTELLAR MATTER 31
   4.1. The Impact 33
   4.2. The Reverse Shock 37
   4.3. X-Ray Emission 39
   4.4. Dust Emission from the Ring 42
   4.5. Radio Emission 43
   4.6. Very-High-Energy Gamma Rays 44
5. HOW UNIQUE WAS SN 1987A? 44

1. INTRODUCTION

This is the third review of SN 1987A in this journal. In the first, Arnett et al. (1989) reviewed the observations made during the first two years after the discovery of the event. Observations of the initial burst of neutrinos were consistent with the notion that the core of the progenitor collapsed and formed a compact object, most likely a neutron star. The optical light curve resulted from diffusion of radiation produced by the decay sequence $^{56}\mathrm{Ni} \rightarrow {}^{56}\mathrm{Co} \rightarrow {}^{56}\mathrm{Fe}$ through the expanding envelope of a massive blue supergiant (BSG) progenitor (mass estimated to be 16–22 $M_\odot$ initially and $\sim$14 $M_\odot$ at the time of explosion). They described the early emergence of gamma rays from the decay of ^{56}Co and of hard X-rays resulting from the Compton scattering of the gamma rays. The observations of narrow UV emission lines first seen with the *International Ultraviolet Explorer* (IUE) satellite indicated the presence of circumstellar matter near [within $\sim$1 light-year (ly)] the supernova (SN), evidently expelled by the SN progenitor.

In the second review, McCray (1993) revisited the evidence that the light curve of SN 1987A was powered by radioactivity and described how it would be dominated at late times by longer-lived isotopes such as ^{57}Co and ^{44}Ti. By $\sim$4 months the SN debris became optically thin in the optical/IR continuum, and its spectrum was dominated by emission lines. Analysis of the nebular spectrum showed that fragments of different elemental composition in the debris had different temperature evolution. By $\sim$200 days, vibration bands of CO and SiO appeared in the IR spectrum, indicating temperatures of $T \lesssim 4{,}000$ K, which decreased to $T \lesssim 2{,}000$ K by $\sim$400 days. In the interval from 400–500 days, dust formed in the debris, rendering most of the inner debris obscure to optical and near-IR (NIR) radiation and converting most of this radiation to the far-IR (FIR) continuum. Images obtained with the European Southern Observatory's New Technology Telescope and the *Hubble Space Telescope* (HST) showed that the nebulosity emitting the narrow UV lines was coming from a system of three circumstellar rings, leading to predictions that the SN blast wave would strike the ring within several years.

In the 23 years that have elapsed since the second review was published, we have learned much about the SN and its evolution, thanks largely to powerful new facilities that have become available in the interim. Despite the fact that its bolometric luminosity has faded by a factor of $\sim 10^7$, SN

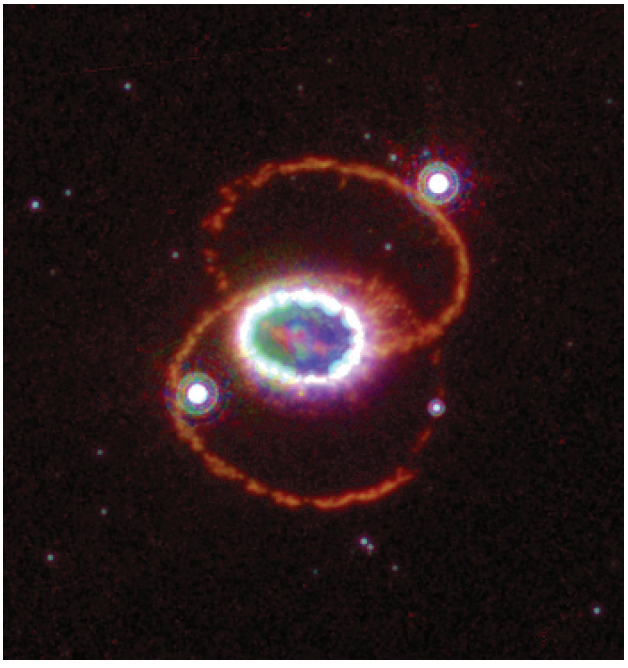

Figure 1

Composite image of SN 1987A in Hα taken with the *Hubble Space Telescope* (HST). Images from three epochs have been stretched and combined to enhance different components. Red, as seen by HST/WFPC2 in 1994–1997; blue, as seen by HST/ACS in 2001–2004; and green, as seen by HST/WFPC3 in 2009–2014. Courtesy of Peter Challis.

1987A is still bright enough to be observed in almost every band of the electromagnetic spectrum. The repaired HST has produced images of the debris and triple-ring system (**Figure 1**) while telescopes empowered with adaptive optics such as the Very Large Telescope (VLT) and the Gemini Observatory have yielded images and spectra far superior to those previously available. The *Chandra X-ray Observatory* (*Chandra*) and *X-ray Multi-Mirror Mission-Newton* (XMM) observatories have tracked the evolution of the image and spectrum of the X-ray-emitting gas. The *International Gamma-Ray Astrophysics Laboratory* (INTEGRAL) and *Nuclear Spectroscopic Telescope* (NuSTAR) observatories have enabled us to observe the predicted gamma rays from the decay of ^{44}Ti. The *Spitzer Observatory* (*Spitzer*) has yielded spectra in the mid-IR (MIR), whereas the *Herschel Observatory* (*Herschel*) gave us the first opportunity to see the SN at FIR wavelengths since 1995, when the Kuiper Airborne Observatory ceased operations. The Australia Telescope Compact Array (ATCA) has tracked the evolution of the image of nonthermal radio emission in the centimeter and millimeter bands. Most recently, the Atacama Large Millimeter Array (ALMA) has enabled us for the first time to resolve the inner SN debris at millimeter/submillimeter wavelengths, free of the obscuration from dust that limits our view in the optical and NIR bands.

Meanwhile, the SN itself has evolved dramatically. Some aspects have proceeded according to script. The predicted impact of the SN debris with its circumstellar equatorial ring (ER) is now fully underway, so that the bolometric luminosity is now dominated by X-ray and MIR emission from the shocked gas and dust in the ring. The luminosity of the inner debris is dominated by the decay of ^{44}Ti. But other aspects have been surprising. "Hot spots" in the HST images showed that the ring contained clumps of gas having density an order of magnitude greater than the average.

Herschel revealed that a substantial fraction of the nucleosynthesis products resides in a massive reservoir of dust in the inner debris, whereas the ALMA observatory has yielded evidence of the presence of CO and SiO molecules having a net mass comparable with the dust mass.

Despite all this progress, mysteries remain. Large departures from spherical or even cylindrical symmetry in both the SN debris and the circumstellar matter still lack satisfactory explanations. Except for the neutrino pulse, no evidence has yet appeared for the compact object that must have formed in the core collapse. In the following, we review this progress and the outstanding issues, concluding with some speculations about future progress that we may expect in future studies of this fascinating and unique phenomenon.

2. ENERGY SOURCES AND LIGHT CURVES

Figure 2 shows the light curves of SN 1987A and its components. The bolometric light curve was dominated by optical light for the first 500 days. By 120 days, the photosphere had vanished, and the light had a "nebular" spectrum, dominated by emission lines, as described by McCray (1993). This optical light tracked the exponential decay ($t_{56} = 111.3$ days) of radioactive energy deposited in the debris until about 500 days, corresponding to a ^{56}Ni mass of 0.069 ± 0.003 $M_\odot$.

At $t \sim 500$ days, a dramatic change occurred in the light curve and spectrum. The optical light rapidly dropped below the ^{56}Co decay luminosity. At the same time, an FIR continuum appeared (Wooden et al. 1993, and references therein). The combined luminosities of the optical light, the FIR continuum, and the escaping gamma rays continued to track the exponential decay of ^{56}Co. Evidently, this change was due to the formation of dust grains within the debris, which absorbed

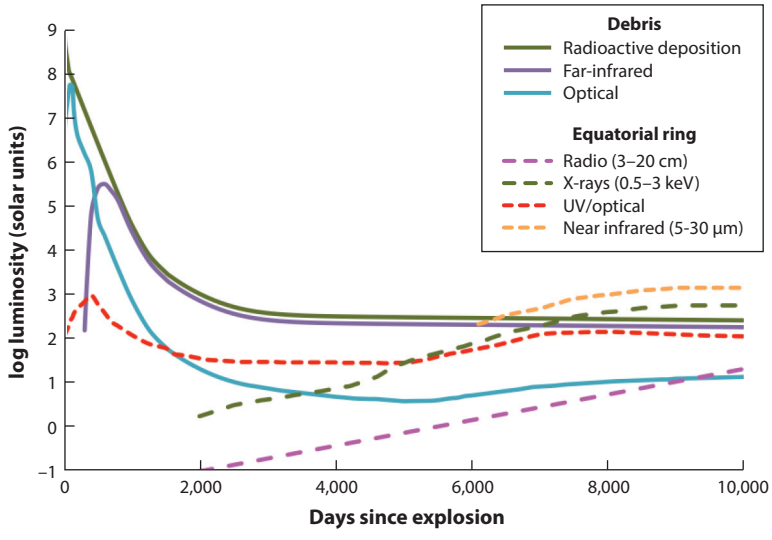

Figure 2

SN 1987A light curves. Solid curves are debris: green, radioactive deposition (Fransson & Kozma 2002, Jerkstrand et al. 2011, Boggs et al. 2015); violet, far-IR (McCray 1993, Matsuura et al. 2015); and cyan, optical (McCray 1993, Larsson et al. 2011, Jerkstrand et al. 2011; J. Larsson, private communication). Dashed curves are the equatorial ring: pink, radio (3–20 cm) (Manchester et al. 2002, Zanardo et al. 2010, 2014, Ng et al. 2013); green, X-rays (0.5–3 keV) (Hasinger et al. 1996, Burrows et al. 2000, Frank et al. 2016); red, UV/optical (Lundqvist & Fransson 1991, Mattila et al. 2010, Fransson et al. 2015); and gold, near-IR (5–30 μm) (Dwek et al. 2008, 2010).

the optical and NIR radiation. The dust grains had temperature $T_d \sim 600$ K (McCray 1993). The red sides of the optical and NIR emission lines nearly vanished, indicating that the dust was almost completely blocking the optical/NIR emission from the far side of the debris.

At roughly the same time, vibration-rotation bands of CO and SiO appeared. Analysis of these bands (Liu et al. 1992, Liu & Dalgarno 1994) indicated that these molecules had masses $M_{CO} \approx 10^{-3}$ $M_\odot$ (Liu et al. 1992) and $M_{SiO} \approx 10^{-3}$ $M_\odot$ (Liu & Dalgarno 1994), respectively. When first detected, at $t = 192$ days, the CO had temperature $T_{CO} \approx 4{,}000$ K, which dropped to $T_{CO} \approx 1{,}800$ K at $t = 377$ days.

Pinto et al. (1988), Woosley et al. (1989), and Hashimoto et al. (1989) predicted that, by $t \approx 1{,}200$ days, the energy deposition in the SN debris would be dominated by the decay of the longer-lived ($t_{57} = 390$ days) isotope ^{57}Co. In addition, as Fransson & Kozma (1993) pointed out, recombination of residual HII ions could make a contribution to the light curve comparable with that from ^{57}Co. They could account for the observed bolometric light curve for $t > 1{,}000$ days with $M_{57} \approx 0.003$ $M_\odot$ of ^{57}Co, close to the value $M_{57} \approx 0.002$ $M_\odot$ predicted by Woosley et al. and Hashimoto et al.

These authors also predicted that the luminosity of SN 1987A would be dominated from $t > 7$ years by the decay of ^{44}Ti ($t_{44} = 85$ years). The radioactive energy is deposited in the debris by fast (596 keV) positrons from the prompt decay of ^{44}Sc, which is the daughter of ^{44}Ti (e.g., Seitenzahl et al. 2009). The estimated ^{44}Ti mass was $M_{44} \approx 10^{-4}$ $M_\odot$. The prediction by Woosley et al. (1989) and Hashimoto et al. (1989) was confirmed with the detection by the INTEGRAL (Grebenev et al. 2012) and NuSTAR (Boggs et al. 2015) observatories of 67.9 keV and 78.4 keV hard X-ray lines, respectively, emitted as a result of the decay of ^{44}Ti (**Figure 3**). The mass of ^{44}Ti inferred from the NuSTAR observation was $M_{44} = (1.5 \pm 0.3) \times 10^{-4}$ $M_\odot$, which is significantly less than the value $M_{44} = (3.1 \pm 0.8) \times 10^{-4}$ $M_\odot$, inferred from the earlier INTEGRAL observation.

In what form does this energy emerge? In a detailed model for energy deposition and spectrum formation, Jerkstrand et al. (2011) estimate a mass $M_{44} = (1.5 \pm 0.5) \times 10^{-4}$ $M_\odot$, which is consistent with the NuSTAR observation. **Figure 4** shows a model fit to the spectrum at ~8 years together with HST observations from Chugai et al. (1997). This ^{44}Ti mass also agrees with a

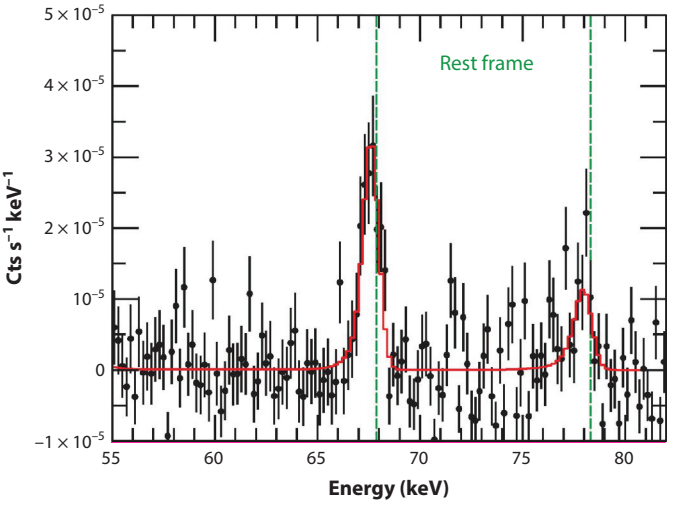

Figure 3

A gamma-ray spectrum of SN 1987A from the *Nuclear Spectroscopic Telescope* (Boggs et al. 2015).

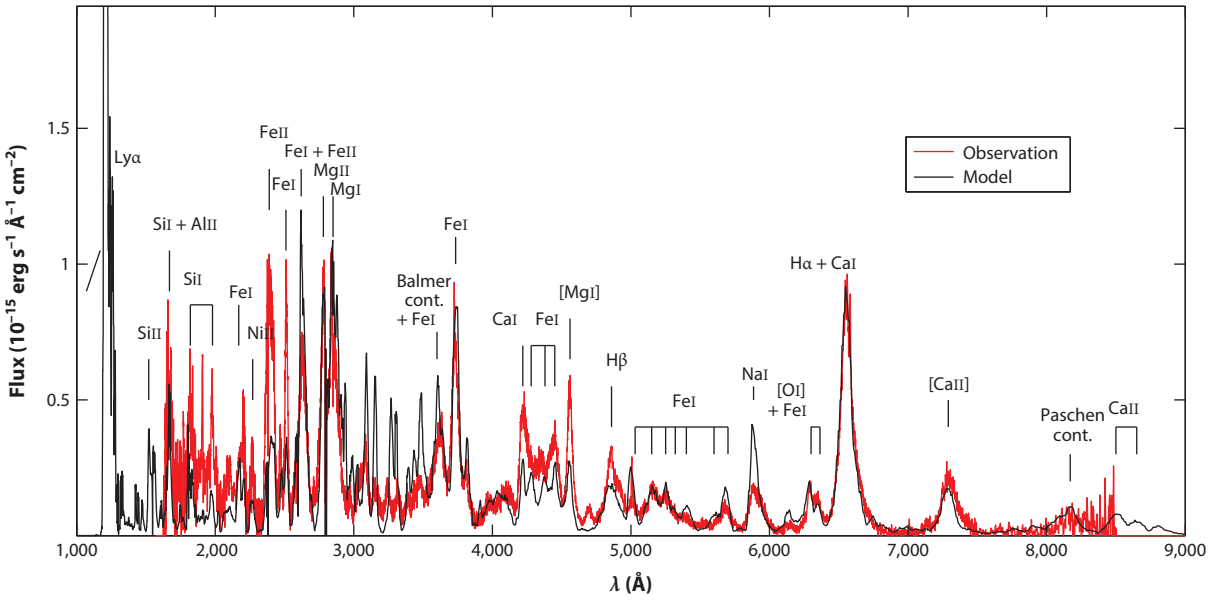

Figure 4

An optical/UV spectrum of SN 1987A at ∼8 years obtained with the *Hubble Space Telescope* (*red*) (Chugai et al. 1997), together with a model spectrum (*black*) (from A. Jerkstrand, private communication, as calculated in Jerkstrand et al. 2011). Note the strong UV emission and the low state of ionization. The optical/UV spectrum at this epoch is dominated by nonthermal excitation and ionization. The ^{44}Ti mass was 1.5×10^{-4} $M_\odot$.

nebular analysis of the FeII emission lines based on the same spectrum by Chugai et al. The spectrum at this epoch is radically different from the thermally dominated spectrum during the first ∼500 days (as discussed in McCray 1993). In the ^{44}Ti-dominated phase the temperature is $\lesssim$200 K, and the only lines that are excited thermally are fine structure lines in the MIR and rotational lines from molecules. All lines in the UV and optical are a result of nonthermal excitation by the fast electrons, resulting from the positrons from the ^{44}Ti decay. The gamma rays from the ^{44}Ti decay escape freely at this epoch, and the total energy input from the positrons at 10,000 days is ∼278 $L_\odot$.

Because of the low ^{44}Ti input the plasma is nearly neutral, as is seen from the strong FeI lines in the spectrum (**Figure 4**). With an electron fraction of ∼0.2, approximately 60% of the positron input goes to heating of the thermal electrons (Kozma & Fransson 1992) while the rest goes to ionization and excitation of UV and optical lines. Jerkstrand et al. (2011) find that most of the heating should be emitted in the [FeII] 26-μm line, resulting in a 26-μm luminosity of $\sim 0.6 \times 278\ L_\odot = 167\ L_\odot$. This is, however, more than an order of magnitude greater than has been observed (Bouchet et al. 2006).

In an observation from *Herschel*, Matsuura et al. (2011) discovered a luminous (∼220 $L_\odot$) source of FIR (100–500 μm) continuum at the location of SN 1987A (**Figure 5**). Lakićević et al. (2012b) confirmed this finding in observations at 350 and 870 μm with the Atacama Pathfinder Experiment. In subsequent observations using the ALMA observatory, Indebetouw et al. (2014) found that the IR source was coincident with the expanding debris. This continuum is evidently produced by dust grains in the debris. A fit to the spectrum showed that the grains have temperature $T_d = 17$–23 K. Matsuura et al. (2015) were able fit the spectrum observed by the *Herschel* and the ALMA, with a model consisting of 0.5 ± 0.2 $M_\odot$ of amorphous carbon or a mix of 0.3 $M_\odot$ of amorphous carbon

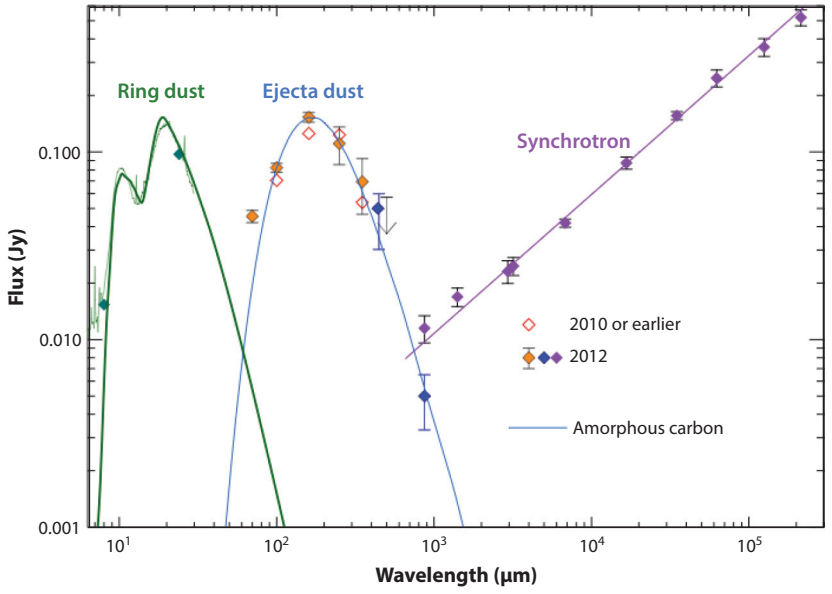

Figure 5

SN 1987A spectral energy distribution (Matsuura et al. 2015). Green, data from the *Spitzer Space Telescope* and fit to silicate emission from the equatorial ring. Orange, data from the *Herschel Space Observatory*. Blue, data from the Atacama Large Millimeter Array. Violet, data from the Australia Telescope Compact Array and the Molonglo Observatory Synthesis Telescope.

and 0.3 $M_\odot$ of silicates, e.g., $MgSiO_3$. More recently, Dwek & Arendt (2015) found that elongated composite grains consisting of ~0.4 $M_\odot$ of silicates and ~0.05 $M_\odot$ of amorphous carbon could account for the FIR spectrum. In any case, the result is astonishing, as it requires almost all of the magnesium and silicon expected from nucleosynthesis models to have condensed into grains.

Such a large mass in grains is sufficient to absorb most of the optical and NIR luminosity produced by radioactive energy deposition in the debris. Depending on its composition and distribution in the debris, the dust may have sufficient optical depth to absorb most of the [FeII] 26-μm line as well. If so, the FIR continuum observed using *Herschel* is a bolometer of the radioactive energy deposition rate.

The FeI-dominated spectrum in **Figure 4** shows, as does the centrally peaked 1.644-μm SiI/FeII emission observed with the integral field spectrograph SINFONI on the VLT (Kjær et al. 2010, Larsson et al. 2013), that the observed optical/NIR spectrum from the core is dominated by reprocessed radiation from the ^{44}Ti radioactivity. Jerkstrand et al. (2011) estimate that of the ~40% of the ^{44}Ti input going into UV/optical/NIR (UVONIR) emission, ~65% is absorbed by the dust, or $\sim 0.4 \times 0.65 \times 278\ L_\odot = 72\ L_\odot$. The remaining ~60% goes to heating, which is mainly balanced by emission in the FeII 26-μm line. The escaping UVONIR luminosity is therefore only ~14% of the total.

Adding up the dust-absorbed energy, one finds a luminosity of $167 + 72 = 239\ L_\odot$, which is within the errors of that derived from the *Herschel* and ALMA dust emissions. One therefore finds a consistent energy budget for the ejecta at these late epochs.

As discussed above, we require the dust to absorb nearly all radiation in the 10–100-μm band. At the same time it must not absorb all the optical/NIR radiation. One possibility is absorption by optically thick silicates, such as $MgSiO_3$ and $MgSiO_4$, which have an opacity in the 10–30-μm

range, which is a factor of $\sim 10^2$–10^3 greater than that at optical wavelengths (Jäger et al. 2003). Corundum (Al_2O_3) has similar optical properties. However, there is evidence for a nearly constant dust absorption in the optical band from ~500 to 10,000 days. Possibly, this is due to a second component of optically thick carbon dust with a covering factor of ~0.65. Silicates, corundum, and carbon dust are the most abundant grains found in simulations of clumpy ejecta by Sarangi & Cherchneff (2015).

A new phase in the energy budget commenced at about day 5,000. Up to this epoch the luminosity of the ejecta had decreased slowly owing to the ^{44}Ti decay. Photometry in the R and B bands with HST, however, showed that after this epoch the luminosity increased steadily by a factor of 3–4 at 10,000 days (Larsson et al. 2011, and J. Larsson private communication). Evidently, X-rays from the ring interaction (Section 4.3) absorbed and thermalized by the ejecta now contribute more to the optical luminosity than the ^{44}Ti decay. Adding up the radioactive contribution and a fraction of ~5% of the X-ray luminosity yields a qualitative agreement with the optical light curves.

This change may be regarded as marking a transition to the remnant phase, when the luminosity is dominated by interaction rather than radioactive input. At the same time the optical morphology changed from centrally dominated emission to a horseshoe-like shape (**Figure 1**) (Fransson et al. 2013). One finds that X-rays with energy of 2 keV can penetrate into the metal core of the ejecta. At this point, the photoelectric absorption by the metals becomes large enough to shield most of the core from the X-rays. It is therefore mainly the hydrogen and helium envelope that is affected by the X-rays. This accounts for the change of morphology of the ejecta in the X-ray-dominated phase.

Because of the greater photoelectric cross section, approximately $\sigma \propto E^{-3}$, X-rays with energy $\lesssim$1 keV are mainly absorbed in the outer parts of the ejecta, close to the reverse shock, which may explain the Lyα emission from this region (France et al. 2015). The X-rays have a similar effect as the positrons and gamma rays. The secondary electrons resulting from the photoelectric absorption lead to excitation, ionization, and heating of the envelope, which result in Lyα, Hα, and IR emission from especially the high-velocity hydrogen envelope (Xu & McCray 1991, Kozma & Fransson 1992).

3. THE DEBRIS

Typical models of a core-collapse SN progenitor have a laminar structure, with nested layers of Si/S, O/Ne, C/O, He, and H surrounding a core of Fe. Instabilities before and after the explosion cause this structure to fragment into "clumps" of different elemental composition that are no longer radially segregated. This mixing is macroscopic, not microscopic, as evidenced by the fact that the temperatures inferred from line ratios of different species are not the same (McCray 1993).

3.1. Optical/IR Emission

During the past decade there has been considerable progress in modeling the early spectra and light curve. In particular, Utrobin & Chugai (2005) have shown that time-dependent effects are important for the ionization of the outer hydrogen envelope. This results in a higher envelope ionization than that in steady state, and is important in order to get a proper strength of the Hα line without invoking clumping or radioactive excitation. This freeze-out of the ionization is analogous to that occurring at very late stages for the inner parts of the ejecta (Fransson & Kozma 1993). Utrobin & Chugai (2005) further show that the overabundance of barium, claimed earlier, can also be explained as a result of the higher ionization in the time-dependent models. The importance of a time-dependent treatment has been confirmed by Dessart & Hillier (2010)

in more detailed models, who also find that there is no need for any extra radioactive source at high velocity to explain the strength of the HI and HeI lines, as has been discussed in early papers. These models probably represent the best reproduction of the spectra and light curve during the first month after explosion, albeit in the context of 1D models.

The formation and diagnostics of the different optical and IR lines in the nebular phase were reviewed by McCray (1993). Fully self-consistent models of the thermal evolution of the different composition zones up to 2,000 days have been calculated by Kozma & Fransson (1998a,b) and de Kool et al. (1998). An important result of these calculations is that the temperatures of the different composition zones differ substantially, depending on the energy input, densities, and compositions. The Fe-dominated zones drop below 1,000 K at ∼500 days, and the Si-rich and O-rich zones somewhat later. The temperature evolves more slowly in the H and He zones, where adiabatic cooling becomes important after 600 days and only reaches 1,000 K by day 1,200. In the metal-rich zones, IR fine-structure lines cause a thermal instability to $\lesssim$200 K in only ∼200 days. This is reminiscent of the "infrared catastrophe" discussed for Type Ia SNe (Axelrod 1980).

Between approximately 800 and 1,500 days, the FeI–II emission is dominated by primordial iron, rather than the synthesized iron, which dominates before and also after this period. The same is true for the [CaII] λ7300 lines, the emission of which is dominated by the O-rich and H-rich zones, not by the Si/S zone, where most of the newly synthesized Ca resides (Li & McCray 1993, Kozma & Fransson 1998a). This is an important lesson for the analysis of other core-collapse SNe. Later than ∼1,500 days, when positrons from ^{44}Ti dominates the energy input, almost all emission is from the Fe-rich zones, except the H and He emission from the slowly recombining envelope.

Although the ejecta in the nebular phase is optically thin in the continua of the excited levels of H and He, it may still have a significant opacity in the many optically thick resonance lines, especially of the Fe group elements (Li & McCray 1996). Even at 8 years there was significant blocking of the UV emission, resulting in a transfer of the UV emission into the optical band by multiple scattering and fluorescence (Jerkstrand et al. 2011).

The models above did not include molecular formation and cooling. In particular, vibrational cooling by CO and SiO can be important in the zones where C/O and O/Si, respectively, are abundant. This was demonstrated for CO by Liu & Dalgarno (1995), who find that in the zone where C is abundant together with O, cooling is dominated by CO. The emission in the fundamental band at 4.6 μm follows the gamma-ray input to the C/O zone, in agreement with observations. This argues against microscopic mixing of He into this zone, where any He^+ would destroy the CO.

Recently, Fransson et al. (2016) have examined NIR spectra with VLT/SINFONI in the K-band between days 6,489 and 10,120 and found clear rovibrational lines of molecular hydrogen, H_2, at 2.12 μm and 2.40 μm. Formation of H_2 was predicted to occur during the first years after explosion by Culhane & McCray (1995) but has not clearly been detected until these very late epochs. The width of the lines, FWHM ∼ 2,300 km s^{-1}, shows that they arise from hydrogen mixed into the core. The excitation of these lines can be caused either by nonthermal electrons and positrons or by the diffuse UV emission in the core of the supernova.

3.2. Ejecta Structure

During the past few decades, substantial progress has been made in understanding the mechanism for core-collapse SNe. Several independent groups have demonstrated that neutrino-driven convection drives large-scale instabilities and can lead to an SN explosion (e.g., Janka et al. 2012). But major uncertainties remain, particularly with respect to the roles of rapid rotation and magnetic fields. Observations of the distribution and kinematics of nucleosynthesis products in the ejecta of SN 1987A offer the possibility of testing and discriminating among theoretical models for the

explosion. As we describe in this section, our knowledge of the structure of the ejecta is still fragmentary, but it is advancing rapidly thanks to new instrumental facilities at several wavelengths.

3.2.1. Observations. Evidence for large-scale asymmetry in the ejecta emerged within a few months of the explosion. Fine structure appeared in the profile of Hα (the "Bochum event") (Hanuschik & Thimm 1990), indicating inhomogeneities in the emission by hydrogen expanding with velocities ~4,500 km s^{-1}. The appearance of X-rays and gamma rays earlier than predicted indicated that some of the newly synthesized ^{56}Co had penetrated into the hydrogen outer layer of the ejecta (McCray 1993).

Wang et al. (2002) have suggested these observations, along with observations of asymmetry inferred from speckle interferometry (Papaliolios et al. 1989) and spectropolarimetry, could be explained if the SN explosion was driven by jets aligned with the major axis of the debris. But it is also possible that these phenomena can be explained without invoking the jet hypothesis.

A unique set of information about the asymmetry at the early epochs, close to maximum light, comes from spectroscopic observations of dust light echoes around SN 1987A (Sinnott et al. 2013). In particular, fine structure in the Hα line, similar to the Bochum event, was seen to vary with the position angle on the light echo rings, indicating an asymmetry in the hydrogen envelope. The direction of the asymmetry agrees well with that inferred from the VLT observations, which, however, refer to the inner metal core.

From images reconstructed through speckle interferometry, Nisenson et al. (1987) reported the detection of a source of optical emission displaced from the SN center by 0.06 arcsec. This so-called "mystery spot" was very bright—only 2.7 mag fainter than the SN at $t = 1$ month. We are unaware of any plausible physical explanation for this phenomenon. If the mystery spot is real, we find it difficult to understand how it could fail to leave any spectroscopic trace of its existence.

Most of the hydrodynamics of the explosion plays out within several hours, except for the expansion of the "nickel bubbles" (Woosley 1988, Herant & Benz 1991, Li et al. 1993), driven by deposition of radioactive energy by ^{56}Ni, which has a mean lifetime of 8.8 days. After a time $\Delta t \sim$ a few weeks, all acceleration had ceased, the debris was coasting, and the structure was expanding homologously. Accordingly, gas in the debris emitting spectral lines having Doppler shift, $V_{\rm D}$, is confined to a thin sheet displaced at a distance $z \approx V_{\rm D}t$ along the line of sight from the center of the explosion, where t is the time since explosion. The sheets of constant Doppler shift are very nearly planar, departing from flatness by $\Delta t/t \sim 10^{-3}$.

Today, the SN debris is quite cold. For example, a fit to the observations of rotational emission lines of CO by Kamenetzky et al. (2013) implies that T(CO) is probably <100 K. It follows that the mean molecular velocity of the emitting gas, $c_{\rm S} \sim (kT/\mu)^{1/2} < 0.2$ km s^{-1}, is far less than the typical expansion velocity of the debris, the emission lines of which have FWHM $\approx$ 3,000 km s^{-1}. Thus, the fractional thickness of a sheet emitting at a given Doppler shift is $\sim c_{\rm S}/V_{\rm D} \sim 10^{-4}$.

The fact that the Doppler shift maps directly to depth enables one to infer the structure of the debris in three dimensions from observations of images within emission lines. A dramatic example of this technique was provided by Kjær et al. (2010) and Larsson et al. (2013), who mapped the debris with the VLT/SINFONI. As **Figure 1** shows, the optical image of the debris at late times is an irregular homunculus elongated in the north-south direction. Most people had assumed that this elongation implied that the debris was prolate, with the north-south extension in the polar direction. If so, the northern lobe of the debris would be red-shifted and the southern lobe would be blue-shifted. But the observations contradicted this picture: The northern lobe was blue-shifted and the southern lobe was red-shifted. These results show that the debris is triaxial, with the northern extension in the plane of the ER and the southern extension in the plane of the sky. The quest to map the debris in three dimensions is confounded by the internal dust,

which is certainly obscuring our view of much of the far hemisphere, as evidenced by the fact that the red wings of the emission lines that vanished when the dust began to form have not reappeared.

In fact, the optical emission from the debris of SN 1987A is now driven primarily by X-rays shining into the debris (Larsson et al. 2011) from shocked gas near the ER. This explanation accounts for the facts that the optical image of the debris has become brighter and appears to be concentrated in the equatorial plane. The dark spot near the center of the optical image (**Figure 1**) could be due to the fact that the soft X-rays do not penetrate to the center and/or due to a dust cloud in the near hemisphere.

With the commissioning of the ALMA, we have a new window on the inner debris. Unlike optical or NIR radiation, millimeter/submillimeter radiation is not absorbed by dust grains. Kamenetzky et al. (2013) observed SN 1987A in early science observations with a partial (14–18 dishes) array in a compact (400-m maximum baseline) configuration and found surprisingly strong emission lines from rotational transitions of CO(1–0, 2–1, and 3–2) and SiO(5–4, 6–5, 7–6, and 8–7) (**Figure 6**). They found that the CO has a minimum mass $M_{\rm CO} > 0.01\ {\rm M}_\odot$ and temperature $T_{\rm CO} = 10$–100 K. This mass is at least an order of magnitude greater than that inferred from the vibrational lines during the first years, $\sim 10^{-3}\ {\rm M}_\odot$ (Liu et al. 1992).

Even without resolving the debris, observations with the ALMA have already given us evidence that the spatial distribution of SiO differs from that of CO. The line profiles are different. Moreover, the SiO line profiles have a "dip" at their centers. This is clear evidence for departure from spherical symmetry in the distribution of SiO.

The ALMA early science observations had angular resolution of ~1 arcsec, which is sufficient to demonstrate that the CO emission originates in the inner debris of SN 1987A but not sufficient to resolve the debris. But when the array is operating at its maximum baseline, it will be able to resolve the CO (2-1) emission with angular resolution of ~0.04 arcsec, which is comparable with the HST. With that resolution, the ALMA should be able to see the kind of structure in the debris predicted in 3D hydrodynamic simulations.

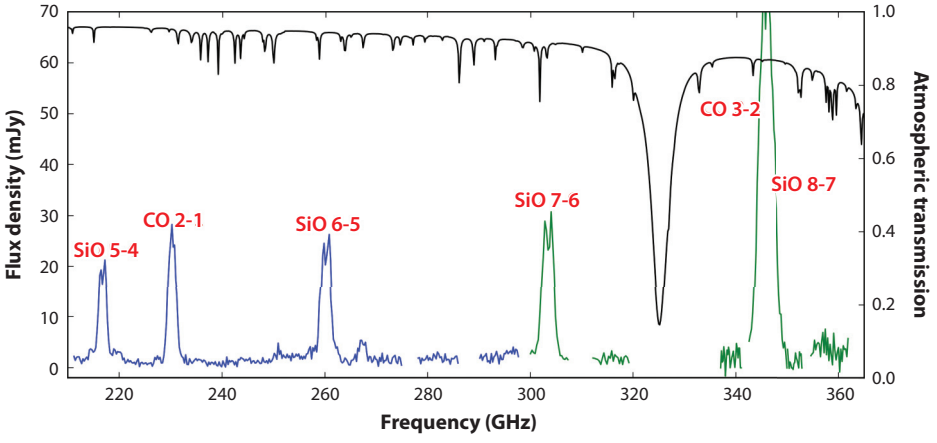

Figure 6

Atacama Large Millimeter Array (ALMA) spectrum of SN 1987A showing bright emission lines from CO ($J = 2$–1), SiO ($J = 5$–4, 6–5, 7–6), and a blend of CO ($J = 3$–2) and SiO ($J = 8$–7), courtesy of M. Matsuura and R. Indebetouw. Note central dips in SiO profiles, which are not prominent in CO profiles. The black curve denotes typical atmospheric transmission at the ALMA site.

3.2.2. Hydrodynamical models. Theoretical models incorporating increasingly realistic physics both for the hydrodynamics and neutrino transport are being developed by several groups (see Janka 2012, Janka et al. 2012, and Burrows 2013 for reviews). Much work remains, however, before one can say for sure that the explosion mechanism is understood. In particular, the interplay between convective motions and nuclear burning during the last burning phases of the progenitor may substantially change the outcome of the explosion (e.g., Herant et al. 1992, 1994; Couch et al. 2015; and references therein).

The observational probes of the explosion mechanism include the neutrino burst; masses and distributions of the radioactive nuclei ^{56}Ni, ^{57}Ni, and ^{44}Ti; other abundant elements, like C, O, and Si; the morphology of the ejecta; and pulsar kick velocities and spins. Pulsar properties and nucleosynthesis yields are sensitive to the explosion mechanism. An important clue is the recent observation by Boggs et al. (2015) that the 68- and 78-keV emission lines from ^{44}Ti decay are red-shifted by 700 ± 400 km s^{-1} relative to the SN rest frame.

There has been some progress in relating the structure and dynamics during the first second to morphology and kinematics that can be observed after the shock breakout. In particular, Hammer et al. (2010) and Wongwathanarat et al. (2015) have made 3D calculations from the core collapse up to the shock breakout. The authors of the latter paper find that the initial structure is significantly affected by the reverse shock and by the asymmetries resulting from the neutrino heating (**Figure 7**).

These authors also find that the structure is sensitive to whether the progenitor is a compact BSG, like that of SN 1987A, or a red supergiant (RSG). In the former case, they also find significant differences between a 15-$M_\odot$ and a 20 -$M_\odot$ progenitor, which is probably related to the different density gradients in the inner core. Their models are only calculated up to less than a day and do not include the heating from the ^{56}Ni decay, which may change the hydrodynamic structure appreciably (Herant & Benz 1991, Li et al. 1993).

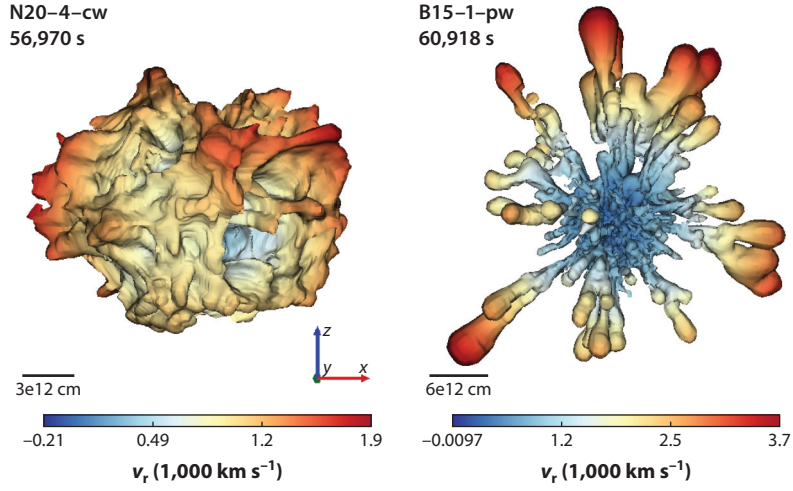

Figure 7

Isocontours at 3% of the ^{56}Ni distribution for a (*left*) 20-$M_\odot$ and (*right*) 15-$M_\odot$ progenitor ~16 h after explosion (Wongwathanarat et al. 2015). The color bars give the expansion velocity of the surface. Note the higher velocities in the strongly fragmented distribution for the 15-$M_\odot$ model. The heating from the ^{56}Ni decay has not been included.

Mapping these 3D models into 1D, Utrobin et al. (2015) have simulated light curves of SN 1987A. They find good agreement of the main diffusion peak at ∼100 days with a 15-$M_\odot$ model. Their results are a major improvement compared to the earlier, artificially mixed models designed to reproduce the light curve. However, their models do not reproduce the early cooling phase during the first days and the general evolution during the first ∼40 days. Another problem is that the core mass of their 15-$M_\odot$ model is too low to explain the progenitor, whereas the 20-$M_\odot$ model, which has the necessary core mass, has too little mixing. The authors suggest a more compact progenitor, possibly indicating a binary origin.

3.3. Dust Formation

There are conflicting scenarios for the dust formation in SN 1987A. Wesson et al. (2015) model the NIR to FIR spectral energy distributions at various epochs for different assumptions about the grain composition and sizes. They find that only ∼0.003 $M_\odot$ of dust could have formed at 1,152 days, the last epoch at which FIR spectra were obtained before 8,467 days, when *Herschel* observations became available. According to their models, the grains are dominated by carbon with only ∼15% of silicates. At the *Herschel* epochs the grains must be large, >3 μm, whereas at the earlier epochs the grains must be at least an order of magnitude smaller. Wesson et al. concluded that most of the grain growth had to take place later than ∼3 years and mainly by coagulation.

In contrast, Sarangi & Cherchneff (2015) find, from detailed kinetic modeling of the dust nucleation and condensation, that most of the grain mass must be formed before ∼1,200 days. For a model including realistic clumping this event occurred even earlier, at ∼500 days. Furthermore, they find that the epoch of formation differed greatly for different species and that the size distribution was very different from that of a standard MRN (Mathis et al. 1977) distribution, as Wesson et al. (2015) had assumed.

According to Sarangi & Cherchneff (2015), most of the dust was in silicates with a smaller fraction of carbon, but it also included pure Mg, Si, and Fe grains. Also the grain sizes and total dust mass were found to be sensitive to clumping. For their clumpy model, they found a total dust mass of ∼0.13 $M_\odot$, whereas a more uniform distribution only gave ∼0.03 $M_\odot$ at the final epoch.

More recently, Dwek & Arendt (2015) proposed a model in which ∼0.4 $M_\odot$ of dust formed at early times, $t \lesssim 500$ days. The grains have ellipsoidal shapes and are composed primarily of silicates with amorphous carbon inclusions. The net masses of refractory elements, ∼0.09 $M_\odot$ of Mg, ∼0.1 $M_\odot$ of Si, and ∼0.046 $M_\odot$ of C, in the grains do not violate expected nucleosynthesis yields. The absence of emission features at 9.7 and 18 μm due to silicates is a consequence of the fact that the dust is optically thick at those wavelengths.

4. CIRCUMSTELLAR MATTER

One of the biggest surprises of SN 1987A was the observation of its system of three circumstellar rings (**Figure 1**). The inner ER is a circle of radius $R_{ER} \approx 0.6$ ly, inclined at 43° (Sugerman et al. 2005). The faint outer loops are roughly coaxial with the inner ring but not coplanar. They have radii about three times that of the inner ring, and their centers are displaced by approximately ±1.3 ly along the cylinder axis.

The rings are glowing because they were ionized by the flash of extreme UV and soft X-rays that lasted a few hours after the SN blast wave emerged from the photosphere of the progenitor. The luminosity of the ring (**Figure 2**) increased to a maximum at about 400 days (Fransson et al. 1989, Sonneborn et al. 1997), which is the time when the ionizing flash illuminated the far side of the ring. Thereafter, the luminosity faded owing to recombination and radiative cooling. Modeling of

the evolution of the UV and optical lines shows that a burst with a radiation temperature of $\gtrsim 10^6$ K is needed to explain the presence of the highest ionization lines of [Nv] (Lundqvist & Fransson 1991, 1996, Mattila et al. 2010). In addition, these authors find a strong He and N enrichment, typical of CNO processing. One can also estimate the mass and density of ionized gas in the ER from the luminosity and fading rate of narrow emission lines from the ring. At first, the ring faded rapidly, indicating that the emission was dominated by relatively high density $n \sim 3 \times 10^4$ cm^{-3} gas, but the fading rate decreased with time, indicating also a lower-density component, $n \sim 1 \times 10^3$ cm^{-3} gas (Mattila et al. 2010). The total mass of gas in the ER that was ionized by the SN flash is $\sim 0.06\ M_\odot$.

Radiation-hydrodynamic models of the shock breakout find a peak temperature of the radiation at $\sim 1.2 \times 10^6$ K with a peak luminosity of $\sim 7 \times 10^{44}$ erg s^{-1} and a decay timescale of less than one hour (Ensman & Burrows 1992, Blinnikov et al. 2000). The equilibrium assumptions behind this modeling have, however, been criticized by Sapir et al. (2013) and Sapir & Halbertal (2014), who find that the rate of photon creation is not fast enough at the shock breakout, so that a Wien spectrum is formed rather than a blackbody.

The inner ring is expanding with radial velocity $V_{\rm ER} = 10.3$ km s^{-1}, which is far too slowly to have been ejected by the SN explosion. Assuming that the ring expands with constant velocity, one may estimate that it was ejected by the SN progenitor at a time $t_{\rm ER} = R_{\rm ER}/V_{\rm ER} \approx 20{,}000$ years before the explosion.

The origin of the outer rings is not understood. The expansion velocity of these relative to the SN is ~ 26 km s^{-1} (Crotts & Heathcote 2000). Tziamtzis et al. (2011) have analyzed HST and VLT observations and find a distance between the outer rings and the SN in the range of 1.7–2.1×10^{18} cm. The facts that the outer loops are roughly 2 times farther from the SN than the ER and are expanding roughly 2.5 times as fast suggests that they were ejected at about the same time as the ER (Crotts & Heathcote 2000). The density of the outer rings is estimated to be $\lesssim 3 \times 10^3 {\rm cm}^{-3}$, which is an order of magnitude lower than the highest densities of the ER but similar to the lower densities dominating the emission at late epochs. In contrast to the ER, the outer rings show a steady decrease in intensity due to the continuing cooling and recombination.

The cylindrical geometry of the triple-ring system suggests that the SN progenitor was a binary star system, and the absence of a star at the explosion site suggests that the stars merged before the explosion. Such a scenario is entirely plausible, given that more than 50% of massive stars belong to close binary systems (Sana et al. 2013). The binary hypothesis also accounts naturally for the fact that the SN progenitor was a relatively compact BSG, not an RSG, star. The merger event could expel a loosely bound outer envelope of a red giant progenitor, much as occurs during the formation of bipolar planetary nebulae (Soker 1998). Morris & Podsiadlowski (2007, 2009) have proposed such a merger model for the formation of the triple-ring system of SN 1987A.

Although the merger scenario is a plausible explanation for the origin of the triple-ring system, the situation is far from settled. Single-star models have been proposed that seem to account for the morphology of the triple ring equally well. For example, Tanaka & Washimi (2002) have proposed a model in which the progenitor is an RSG star having a stellar wind with an embedded magnetic field. The field is wrapped into a toroidal field by the stellar rotation, and the resulting pinch effect confines a dense neutral sheet plasma in an equatorial disk. Magnetic pressure also causes a density enhancement at midlatitudes. After the progenitor makes its transition to a BSG, the fast BSG wind inflates a bubble that concentrates the density enhancements of the BSG wind into the triple-ring system.

Alternatively, Chita et al. (2008) have proposed a purely hydrodynamic model based on a rapidly rotating 12-$M_\odot$ progenitor. The rapid contraction as the star transitions from the RSG

stage to the BSG stage and a corresponding increase of the rotational velocity at the surface lead to a centrifugal ejection of a flattened torus, which is later compressed into the ER. The rapid rotation in the BSG stage also leads to a highly anisotropic wind with most of the mass loss and highest wind velocity in the polar direction. The breakout of this wind from the shell expelled by the RSG wind may give rise to a density enhancement at the interface between these components and explain the two outer rings. Whether the same scenario also can be applied to more massive progenitors remains to be seen.

Most recently, rapid rotation has been invoked in a single-star scenario by Sukhbold et al. (2015) to explain the observed properties of the progenitor. Their best-fit model has a zero-age main sequence mass of 18 $M_\odot$ and a rotational speed of 240 km s^{-1} on the main sequence. During the last 15,000 years it evolves from an RSG to a BSG, at which point it explodes. The final total mass is 16.9 $M_\odot$, and the O mass is 1.25 $M_\odot$, in rough agreement with that determined from nebular modeling (Fransson & Kozma 2002). Although the progenitor luminosity is somewhat high, they find that this is sensitive to the angular momentum, and a decrease by 25% would bring it down to the observed value. They claim that 18 $M_\odot$ is the highest possible progenitor in terms of the He core mass. They do not discuss the formation of the ring system, but a similar scenario as that of Chita et al. (2008) may be possible.

Many uncertainties remain regarding the distribution of circumstellar matter. For example, how is the structure of the ejected matter modified by the ionizing radiation and stellar wind of the BSG progenitor? To explain the early radio emission, Chevalier & Dwarkadas (1995) proposed that the ionizing radiation from the progenitor would produce an HII region of density $n \approx 10^2$ cm^{-3} bounded on the inside by the shocked stellar wind of the progenitor and on the outside by the ER. **Figure 8** shows a schematic figure of the structure of the circumstellar medium around the progenitor with the interacting winds and the HII region.

An upper limit of ~200 cm^{-3} for the HII region was derived from the low flux of NVλ1240 at 1,600–1,800 days after the explosion (Lundqvist et al. 1999). Consistent with this, a component with a density of ~100 cm^{-3} and a mass of ~0.02 $M_\odot$ was found to be needed to explain optical lines at ~5,000 days (Mattila et al. 2010).

Even more mysterious is the distribution of circumstellar matter beyond the triple-ring system detected through echoes of the SN light reflected by dust grains. Sugerman et al. (2005) have constructed a detailed model for the distribution of this matter assuming that it has cylindrical symmetry along the axis of the triple-ring system and reflection symmetry about the plane of the ER. The structure has an hourglass shape, having a radius of ~3 ly in the equatorial plane and extending to ~20 ly in the polar directions. The estimated total mass of gas and dust is ~1.7 $M_\odot$. It seems likely that this structure was ejected by the progenitor system some time before the triple-ring system, but, as yet, no model has been proposed for its formation. Because no spectral lines were detected from the structure, we have no evidence for its kinematics or age. The fact that the blast wave has now advanced beyond the ER (Section 4.2) gives us hope for probing this region in the future.

4.1. The Impact

Soon after the discovery of the circumstellar rings, people realized that a spectacular display would ensue when the SN blast wave struck the ER. The date when this crash would begin depended on the model for the density structure of the outer envelope of the SN and on the distribution of circumstellar matter inside the ER. Estimates ranged from ca. 1999 (Luo et al. 1994) to ca. 2005 (Chevalier & Dwarkadas 1995).

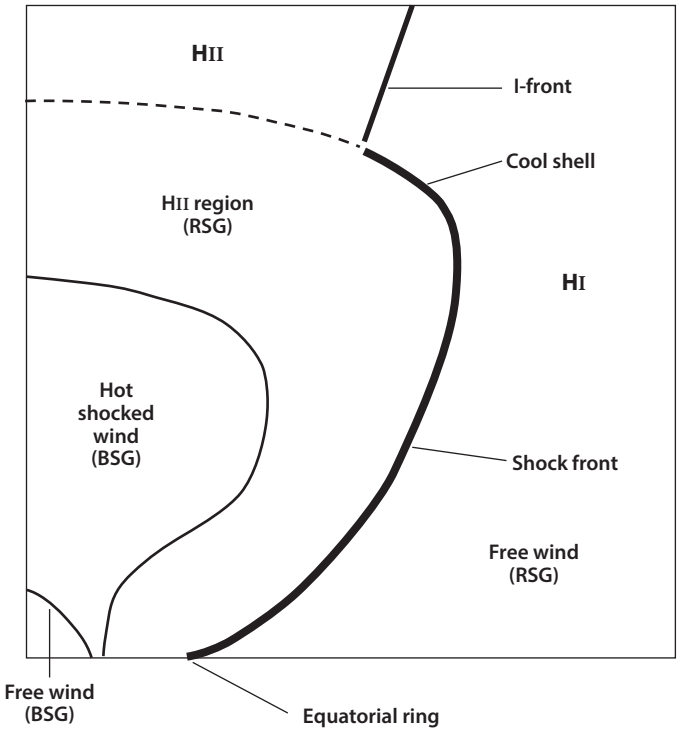

Figure 8

Schematic of the circumstellar HII medium of Sanduleak −69° 202 before the explosion (Chevalier & Dwarkadas 1995). Abbreviations: BSG, blue supergiant; RSG, red supergiant.

In fact, evidence that this crash was beginning first appeared in 1995 as a rapidly brightening hot spot (Spot 1) on the north-east quadrant of the ER (Sonneborn et al. 1998, Lawrence et al. 2000). This event was followed a few years later by the appearance of three more spots on the south-east quadrant. By January 2003 the ER was fully encircled by hot spots, of which there are now ∼30 (**Figure 9**).

The spots are moving radially outward, with longitudinal velocities (inferred from Doppler shifts) and transverse velocities (inferred from proper motions) extending up to ∼700 km s^{-1} (Fransson et al. 2015). Evidently, the hot spots are the result of shocks propagating into dense clumps of gas in the ER.

We interpret the interaction of the SN with the ER in the context of a schematic model illustrated in **Figure 10**. The central structure represents the nucleosynthesis products and the internal dust. They are surrounded by the freely expanding outer envelope of the SN composed mostly of hydrogen and helium (rendered *blue* in **Figure 10**). This envelope is suddenly decelerated at a reverse shock (the *blue-yellow* interface) and heated to temperatures of $\sim 10^7$ K. The shocked envelope drives a blast wave into the ER, which consists of slowly expanding gas that was photoionized by the ionizing flash from the initial SN shock breakout (rendered *red*) and by fingers of relatively dense gas (rendered *white*). As the blast wave overtakes these fingers, transmitted shocks give rise to soft X-ray and optical emission, manifested as hot spots, while reflected shocks heat and compress the debris further and give rise to a higher-temperature component of X-ray emission.

Figure 11 shows a recent high-dispersion spectrum obtained with the VLT, showing the different spectral components of the ejecta and shock interaction. The broad Hα wings with velocities

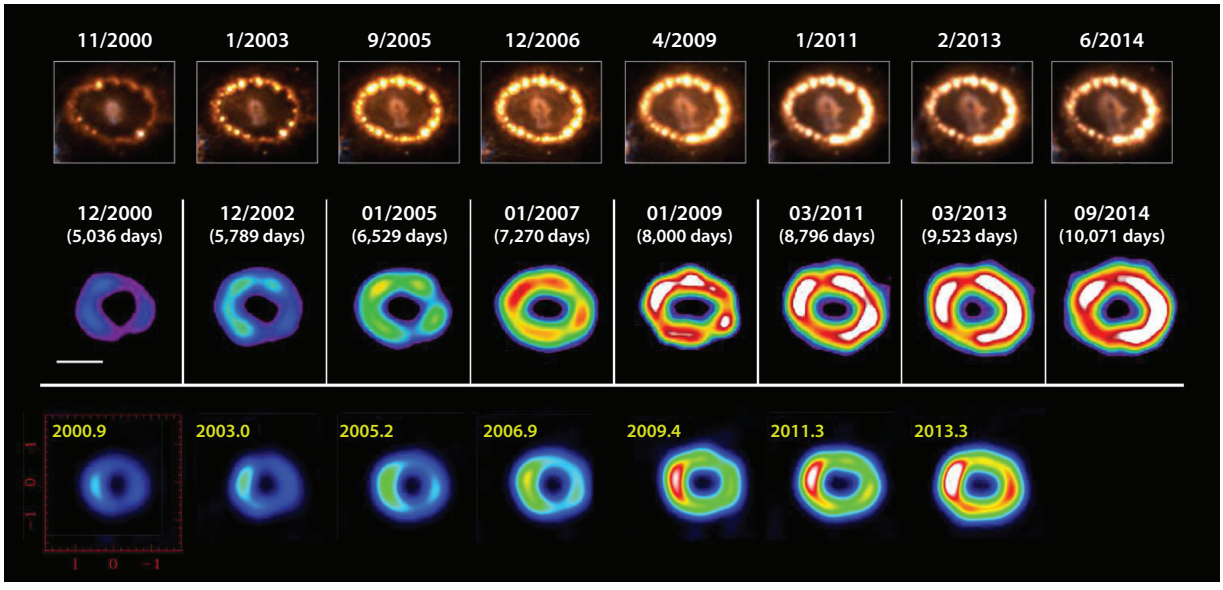

Figure 9

The evolution of SN 1987A and its equatorial ring. (*Top row*) Optical (Fransson et al. 2015). The brightness of the ring has been reduced by a factor of 20 to make it possible to see faint emission from the SN debris and beyond the ring. (*Middle row*) 0.5–3 keV X-rays (Frank et al. 2016). (*Bottom row*) 9 GHz (Ng et al. 2013).

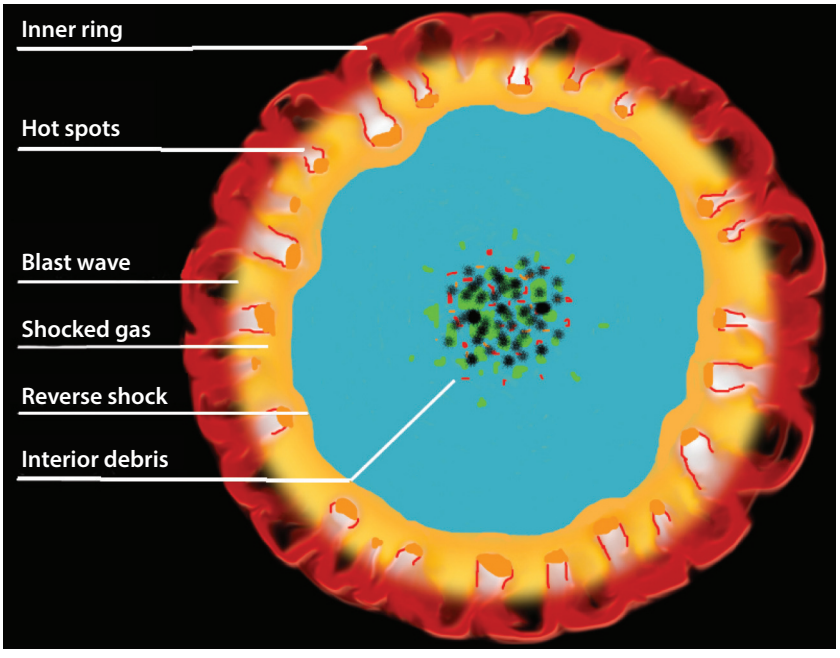

Figure 10

Diagram illustrating the interaction of the supernova debris with the equatorial ring.

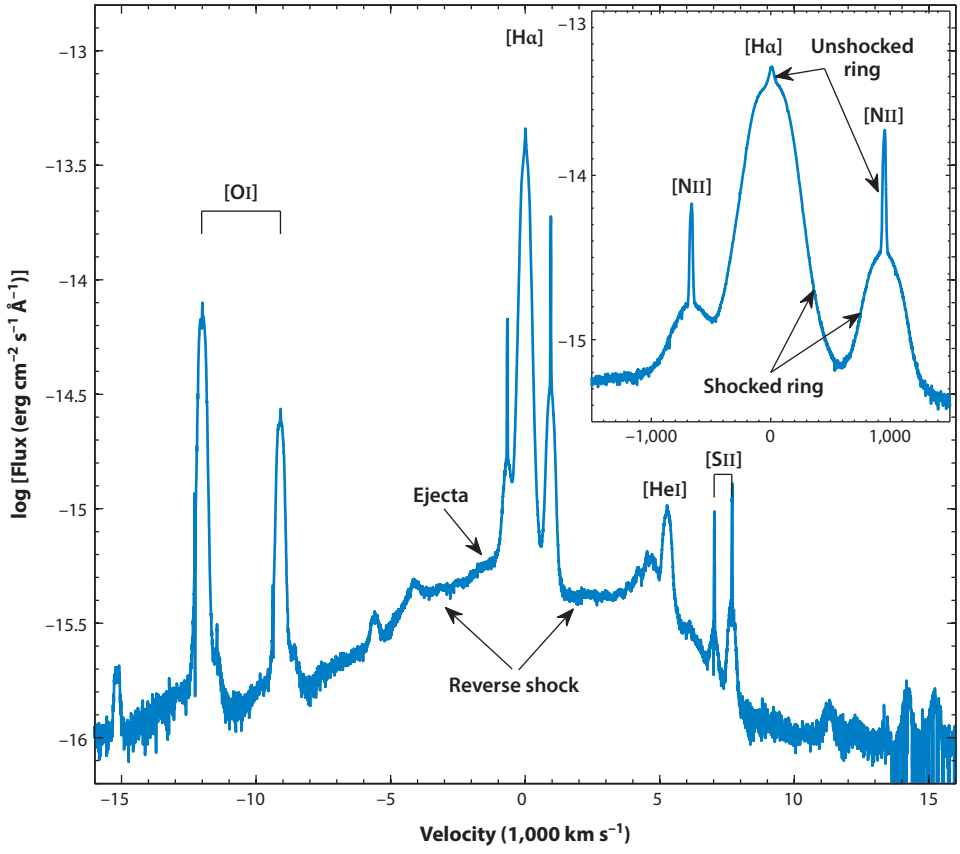

Figure 11

The different spectral components of the ejecta and circumstellar medium interaction as seen in the Hα and [NII] lines with VLT/UVES in 2013 (K. Migotto, private communication). The inset shows a magnification of the $\pm$1,500 km s^{-1} region around Hα. Also the [OI] lines at 6300 Å and 6364 Å have both an ejecta and a shocked ring component.

up to ~10,000 km s^{-1} come from neutral hydrogen crossing the reverse shock, whereas the intermediate component with velocities up to ~700 km s^{-1}, seen more clearly in the inset, originates from the shocked clumps in the ring. The narrow lines with FWHM ~ 10 km s^{-1}, seen most clearly in the [NII] lines, come from the unshocked ring material. Weak emission from the ejecta with FWHM ~ 2,000 km s^{-1} is seen on the blue side of the intermediate velocity Hα and [NII] lines.

To be visible optically, the shock must be radiative; i.e., the radiative cooling timescale of the shocked gas must be less than the timescale for the shock to propagate through the clump. The cooling time is $t_{\rm cool} \approx 38(V_s/500\ {\rm km\ s^{-1}})^{3.4}(n_e/10^4\ {\rm cm^{-3}})^{-1}$ years. As time progresses, shocks with increasing velocity will therefore become radiative. This can be seen in the maximum width of the Hα line, which has increased from 550 km s^{-1} in 2007 to ~800 km s^{-1} in 2013 (Gröningsson et al. 2008; K. Migotto, private communication). For a given pressure driving the shock, the above condition sets a lower density limit, $n_{\rm crit} \approx 10^4$ cm^{-3}, for a clump to become radiative (Pun et al. 2002). If the density falls short of this threshold, the shock will heat the clump to a temperature of $>10^6$ K, at which the shocked gas will emit soft X-rays and very little optical radiation (except for faint coronal emission lines from [FeIX–XIV] (Gröningsson et al. 2006)). Thus, the passage of the blast wave

through the ring will illuminate the dense clumps at high contrast, erasing the narrow line emission from the unshocked ring and creating an increasing luminosity of soft X-rays. A hot spot will disintegrate in a timescale comparable with the time for a shock to pass through a clump as a result of hydrodynamic instabilities that shred the cooling layer behind a radiative shock (Pun et al. 2002).

The driving pressure of the shocks propagating into the ring is determined by the ram pressure of the outer envelope of the debris flowing through a reverse shock that lies inside the blast wave. Because the density of this envelope is believed to have a steep gradient, $\rho \propto r^{-n}$, where $n \approx 8.6$, this pressure will increase with time as $P \propto t^{3.6}$ if the reverse shock is stationary. It follows that the critical density for the clumps to become radiative will also increase with time, roughly as $n_{\rm crit} \propto t^2$. If, as seems plausible, the distribution of clumps is a decreasing function of density, fewer hot spots will appear as time progresses.

This scenario is consistent with observations (Fransson et al. 2015). The light from the hot spots reached a maximum at about 7,000 days on the eastern side of the ER and about 8,000 days on the western side and then began to fade, whereas the X-rays continued to increase (**Figure 2**). A few new hot spots have appeared outside the ring, evidently due to the blast wave overtaking new clumps (**Figure 1**).

By 1994, before the hot spots appeared, the HST images of the ER were dominated by relatively low-density ($n \sim 10^3$ cm^{-3}) gas. When they first appeared, the hot spots were found inside the ER, at radial distances typically 5% less than that of the radius of the ER seen in the HST images (Fransson et al. 2015). This fact is a natural consequence of the action of the progenitor wind on the circumstellar matter, which would push away lower-density gas and leave the higher-density clumps behind, as is seen in planetary nebulae such as the Helix Nebula (O'Dell & Handron 1996).

The fact that the brightest hot spots lie inside the ER has an interesting implication regarding the distance of SN 1987A. In principle, this distance can be determined by dividing the physical diameter of the ring by its angular diameter. The former can be inferred from observations obtained by the IUE of the rise and fall of the narrow line emission from the ring during the first year after the SN outburst. Panagia et al. (1991) used this technique to estimate that SN 1987A was at a distance of 51.2 ± 3.1 kpc (cf. Gould & Uza 1998). However, the angular diameter measured from the HST images is that of the ring of low-density gas, whereas the light curves of the narrow emission lines seen with the IUE were probably dominated by emission from the ring of high-density clumps that are now seen as hot spots. If so, the estimated distance to SN 1987A should be increased by ~5%.

4.2. The Reverse Shock

The impact of the outer envelope of SN 1987A with its circumstellar matter establishes a complex hydrodynamic structure, bounded on the inside by a reverse shock, where the freely expanding outer envelope of the SN debris is suddenly slowed and heated, and on the outside by a blast wave, where the nearly stationary circumstellar matter is suddenly accelerated. The shapes of the reverse shock surface and the blast wave are determined by the density distribution of circumstellar matter, much of which is uncertain. When the blast wave encounters a density discontinuity, it slows down suddenly and sends a reflected shock back into the shocked gas between the reverse shock and the blast wave. The reflected shock from the ER will merge with the reverse shock, creating a nearly stationary bow shock and pinching the reverse shock into an hourglass shape. At higher latitudes the shape of the reverse shock is probably determined by the shape of the HII region described by Chevalier & Dwarkadas (1995) (**Figure 8**).

It is possible to map the reverse shock in three dimensions through imaging spectrometry (**Figure 12**). Hydrogen atoms crossing the reverse shock will emit Hα and Lyα photons when

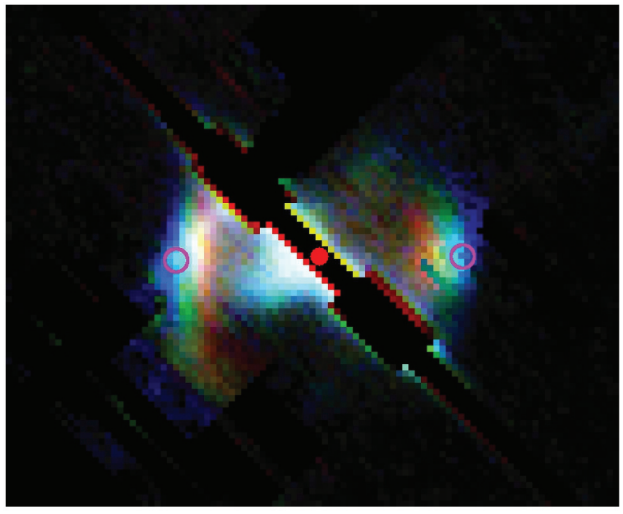

Figure 12

Images of Hα emission from the reverse shock surface, transformed from HST/STIS spectra (P. Challis, private communication). The slit (0.2 arcsec) is centered on the SN (denoted by a *red dot*) and oriented in the north-south direction. The horizontal dimension is line-of-sight depth inferred from Doppler shift. The observer direction is to the left. The vertical streaks manifest the reverse shock at three epochs: red, 2004; green, 2010; and blue, 2014. The reverse shocks are clearly expanding toward the equatorial ring (denoted by *purple circles*). Blue-shifted Hα emission from the inner debris is also evident. Emission from the stationary ring is masked out.

they encounter the ionized plasma downstream from the shock (Borkowski et al. 1997). The emitted photons will have Doppler shifts corresponding to the freely streaming atoms before they cross the shock, so that Doppler shifts map into depths along the line of sight. It is also possible to infer the flux of HI atoms through the reverse shock surface, because each atom crossing the reverse shock will emit, on average, 1 Lyα and 0.2 Hα photons before it is ionized.

Michael et al. (1998, 2003), Heng et al. (2006), and France et al. (2010, 2011) have employed the STIS (Space Telescope Imaging Spectrograph) on the HST to map the reverse shock near the ER where it is brightest. The main results of these studies include the following:

1. The Hα emission is dominated by the reverse shock inside the ER, as expected.
2. The observations show substantial departures from cylindrical symmetry, with the near (north) side of the ring brighter than the far (south) side by $\sim$30%.
3. Near the ER, the reverse shock surface is moving outward with radial velocity of $\sim$2,500 km s^{-1}.
4. The flux of Hα photons has increased steadily, by a factor of $\sim$7 in the interval from April 1997 to January 2010.
5. The flux of Lyα photons has increased more rapidly than that of Hα.
6. In some locations, the photon ratio $R_{\rm LH}$ = Lyα/Hα exceeds the predicted value $R_{\rm LH} = 5$ by a factor of $>$2.
7. Unlike the Hα emission, the Lyα emission is not confined to the reverse shock surface but dominated by emission interior to this surface (**Figure 13**).

Far from the equatorial plane, the reverse shock is too faint to see with the STIS. Instead, France et al. (2015) obtained images of this faint emission with the Wide Field Camera of the HST in combination with filters that select highly red- and blue-shifted Hα emission. An extension of

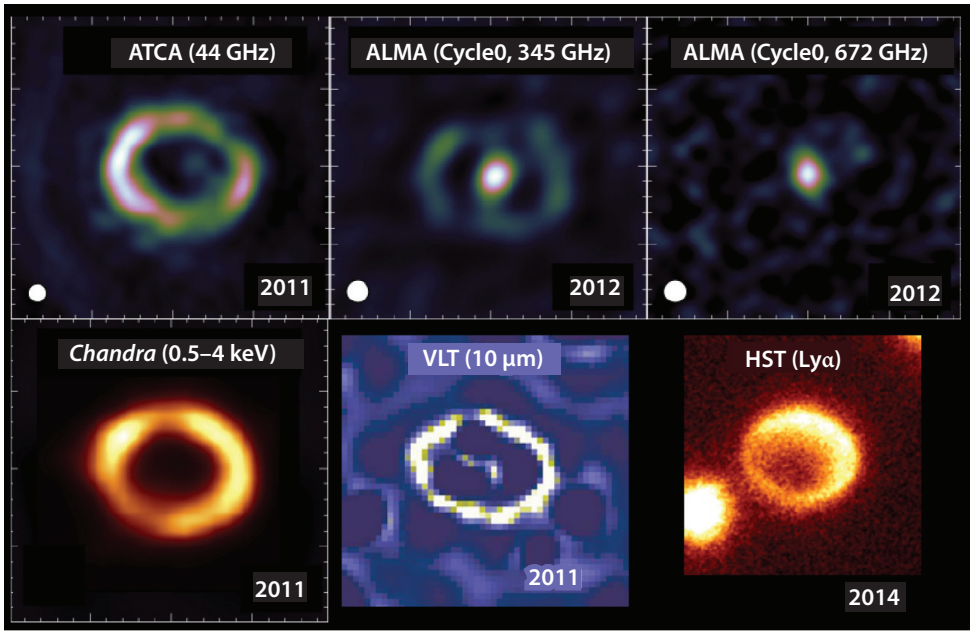

Figure 13

Multiwavelength images of SN 1987A from: (*top row*) the Australia Telescope Compact Array (ATCA) and the Atacama Large Millimeter Array (ALMA) (Indebetouw et al. 2014); (*bottom row*) the *Chandra X-ray Observatory* (*Chandra*) (Frank et al. 2016), the Very Large Telescope (VLT) in January 2011 (Bouchet & Danziger 2014), and the *Hubble Space Telescope* (HST) in June 2014 (France et al. 2015).

the reverse shock substantially out of the ring plane is consistent with spectra obtained from the VLT (Fransson et al. 2013), which show Hα emission extending to $\gtrsim$10,000 km s^{-1}, whereas the maximum velocity in the ring plane is $\sim$4,500 (25 years/t) km s^{-1}.

If the flux of ionizing photons into the debris exceeds the flux of HI atoms through the reverse shock, it can suppress the Hα emission from the reverse shock. Smith et al. (2005) predicted that this suppression may occur sometime around 2015, but we have not yet seen any evidence of this phenomenon (Fransson et al. 2013).

Evidently, the Lyα emission is dominated by a mechanism other than excitation of HI atoms crossing the reverse shock surface. The most likely candidate is thermal excitation by electrons heated by external X-rays penetrating into the unshocked debris. If the debris has ionization fraction $n_e/n_{\rm H} > 0.03$, most of the energy deposited by X-ray photoionization will heat the electrons, and thermal excitation of HI will produce Lyα without much Hα, explaining the large observed value of $R_{\rm LH}$. The fact that the asymmetry of the Lyα image tracks that of the X-ray image (**Figure 13**) supports this interpretation.

4.3. X-Ray Emission

About four months after the explosion, the *Ginga* satellite detected a source of hard ($\sim$25 keV) X-rays from SN 1987A. As discussed by McCray (1993), these X-rays emerged from the SN debris as the result of down-Comptonization of gamma rays from ^{56}Co decay.

Figure 2 shows the light curve of soft (0.5–2 keV) X-rays. They were first detected by the *Röntgensatellit* (ROSAT) in February 1991 (day 1,448) and increased steadily until day 3,013 (Hasinger et al. 1996). When first observed with *Chandra* on day 4,608, the soft X-ray flux

exceeded a linear extrapolation of the ROSAT light curve by a factor of ∼1.6 (Burrows et al. 2000). Thereafter, the light curve increased exponentially, from ≈10 $L_\odot$ on day 4,300 to ≈500 $L_\odot$ on day 8,600. The light curve appears to have begun to level off since then (Frank et al. 2016).

The soft X-ray image (**Figure 13**) is an irregular torus. When first observed with *Chandra*, it was brightest on the east side, but after the impact was well underway, the image resembled that of the optical hot spots, except that the angular resolution was lower. Before day 6,100, the image was expanding with a radial velocity of ∼8,500 km s^{-1}(Racusin et al. 2009); thereafter, the expansion velocity slowed to ∼1,850 km s^{-1} (Helder et al. 2013). Evidently, the X-ray emission is related to the same shock system that gives rise to the optical hot spots.

High-resolution X-ray spectra of SN 1987A (**Figure 14**) have been obtained with *Chandra* (Michael et al. 2002; Zhekov et al. 2005, 2006; Dewey et al. 2008) and with the XMM (Sturm et al. 2010). The spectra are dominated by emission lines from K-shell transitions of H- and He-like ions of N, O, Ne, Mg, Si, and S and L-shell transitions of FeXVII–FeXX (**Figure 14**). The picture that emerges from the grating spectra is complex. A bimodal distribution function of emission measures versus temperature, with peaks at ≈0.5 keV and ≈2.0–2.5 keV, is required to fit the line ratios. (The temperature of the hot component is decreasing with time.) Fitting an expanding ring model to the X-ray line profiles gives a radial expansion velocity of ∼300 km s^{-1}, which is much less than the value of ∼1,850 km s^{-1} inferred from the proper motion of the expanding X-ray image. Evidently, the low-temperature component of the X-ray emission is dominated by shocks transmitted into clumps of relatively high-density gas (which also produce the optical and UV emission from the radiative shocks), whereas the high-temperature component is dominated by faster shocks reflected off these clumps. The fact that the expansion velocity deduced from proper motion of the X-ray image exceeds that deduced from the X-ray line profiles suggests that the dense clumps are in fact radial fingers of gas being overtaken by the blast wave.

Orlando et al. (2015) have recently modeled the X-ray evolution from the time of the explosion up to 40 years, using a high-resolution adaptive mesh hydrocode. Their 3D simulation includes the ejecta (with clumpiness put in by hand), the wind of the progenitor, an HII region of constant density, and an ER (similar to that in **Figure 8**). The ER includes both clumps of high density and a smooth inter-clump medium of lower density. The adaptive mesh is crucial in order to resolve both the interaction with the clumps at small scales and the large-scale interaction with the HII region. From the resulting hydrodynamic structure, they calculate the X-ray emission, taking departures from ionization equilibrium and electron-ion temperature equilibrium into account.

In **Figure 15**, the resulting soft and hard X-ray light curves are shown with contributions from the different components, compared with ROSAT, *Advanced Satellite for Cosmology and Astrophysics* (ASCA), *Chandra*, and XMM observations. The emission up to 15 years is dominated by the interaction with the HII region. When the ejecta starts to interact with the ring, this dominates the emission until ∼32 years. The soft X-rays are dominated by the clumps, whereas the hard X-rays mainly come from the interaction with the smooth component. In the soft X-rays the contribution from the ring is predicted to peak at ∼27 years, and at somewhat later time for the hard X-rays. It then declines, similar to what is already observed in the optical (Fransson et al. 2015). As discussed earlier, it would not be surprising to find a correlation between the soft X-rays and optical emission from the hot spots. In the final phase, when the blast wave has propagated past the ring, the X-ray emission is mainly coming from the reverse shock, heating the envelope of the ejecta. The morphology in this phase is characterized by bright knots of shocked ejecta clumps.

The parameters of the circumstellar medium and ring for their best-fit model agree well with those determined from the optical and X-ray observations. The evolution during the HII region phase is sensitive to the density profile of the ejecta and is best reproduced for a $\rho \propto V^{-8}$ profile. This is similar to indications obtained from models of the early light curve.

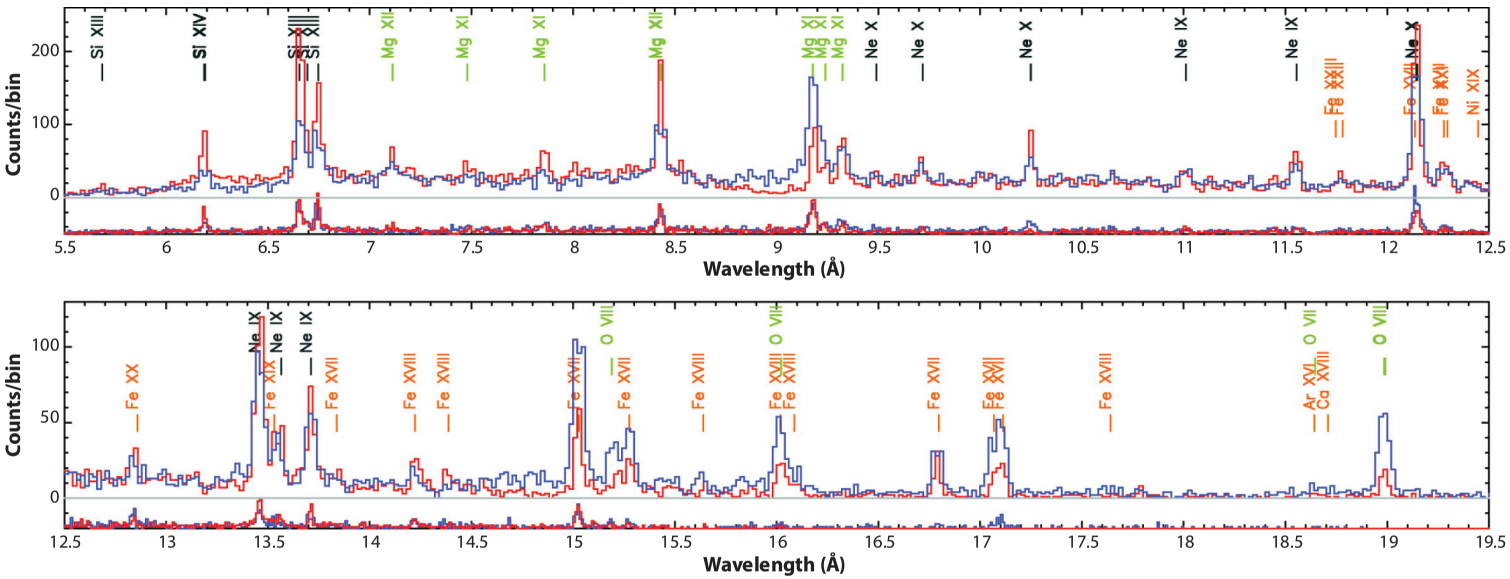

Figure 14

Chandra High Energy Transmission Grating (HETG) spectrum of SN 1987A, March 2007. Upper spectrum is from the Medium Energy Grating, with red (blue) indicating +1 (−1) orders. Lower spectrum is from the HETG (same color coding). Reprinted from Dewey et al. (2008) with permission.

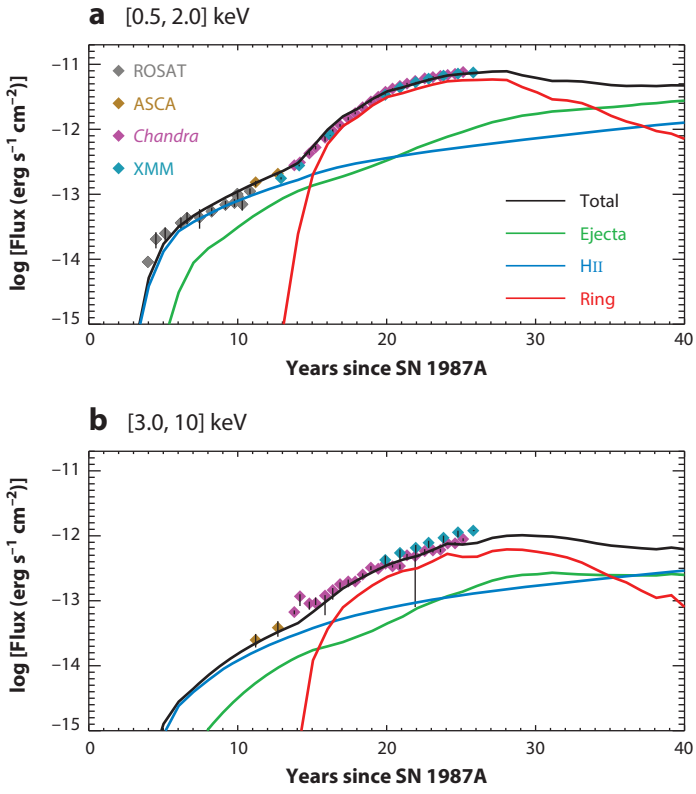

Figure 15

A simulation of the (*a*) soft and (*b*) hard X-ray evolution of SN 1987A compared with observations (Orlando et al. 2015). The contributions from the different emission components are shown separately for each of these bands. Abbreviations: ROSAT, *Röntgensatellit*; ASCA, *Advanced Satellite for Cosmology and Astrophysics*; *Chandra*, *Chandra X-ray Observatory*; XMM, *X-ray Multi-Mirror Mission-Newton*.

4.4. Dust Emission from the Ring

If circumstellar gas containing dust grains is heated to temperatures of $\gtrsim 10^6$ K, the dust grains can be heated by collisions with electrons and ions and will radiate this heat as IR continuum. If the gas has cosmic abundances of refractory elements typical of interstellar gas and a substantial fraction resides in grains, the emission of IR radiation by the grains is more efficient than the emission of X-rays by electron-ion collisions. This is the case for many SN remnants (Dwek & Arendt 1992), and it is true for SN 1987A as well.

Infrared Space Observatory observations at $t \sim 3{,}900$ days showed a marginally resolved source at 6.8–14.3 μm (Fischera et al. 2002a). Both the size and elongation argued for an origin from the region of the ring. With the *Spitzer* telescope, Bouchet et al. (2006) and Dwek et al. (2008) observed the spectrum of IR emission from SN 1987A in the MIR (5–30 μm) band at two epochs, $t = 6{,}190$ days and $t = 7{,}137$ days (**Figure 5**). Bouchet et al. (2006) and Bouchet & Danziger (2014) also obtained diffraction-limited images of SN 1987A at 10 μm (**Figure 13**), showing clearly that the MIR radiation was coincident with the X-ray image.

Dwek et al. (2008) presented a detailed study of this emission and showed that it could be modeled with a plane-parallel shock entering circumstellar gas having density ~ 0.3–1×10^4 cm^{-3}

containing silicate grains having Large Magellanic Cloud interstellar abundance (∼0.3 times cosmic abundance). Collisions with electrons and ions in the shocked plasma ($T \approx 3.5 \times 10^6$ K) heat the grains to ∼180 K. The ratio of MIR to X-ray continuum luminosity decreased from $IR/X = 3.8 \pm 0.6$ at $t = 6{,}184$ days to $IR/X = 2.7 \pm 1.0$ at $t = 6{,}582$ days, evidently owing to destruction of the grains by sputtering in the X-ray-emitting plasma (Dwek et al. 2010; see also **Figure 2**). Dwek et al. also find evidence that dust grains smaller than ∼0.02 μm were evaporated by the initial UV/soft X-ray flash (Fischera et al. 2002b).

4.5. Radio Emission

SN 1987A has been observed since the event using the Molonglo Observatory Synthesis Telescope (Turtle et al. 1990, Ball et al. 2001) at 36 cm and the ATCA at 3–20 cm since the mid-1990s (e.g., Manchester et al. 2002, Zanardo et al. 2010, Ng et al. 2013). The radio remnant has been imaged with the ATCA at 3 mm by Lakićević et al. (2012a) and, more recently, at 3.2 mm and 450 μm with the ALMA (Indebetouw et al. 2014, Zanardo et al. 2014).

The radio remnant appears as a torus; however, its evolution and morphology differ substantially from the optical and X-ray images (**Figure 9**). From day ∼5,000 to day ∼8,000, the radio luminosity at 3–35 cm (**Figure 2**) increased exponentially with an e-folding time of $2{,}408 \pm 227$ days (Zanardo et al. 2010). Since then, the radio remnant has continued to brighten, but at a slower rate (Staveley-Smith et al. 2014). In contrast to the X-rays, no sharp break in the radio light curve was evident at $t \sim 6{,}000$ days, when the optical hot spots appeared. Likewise, the radial expansion velocity of the radio image did not decelerate rapidly when the optical hot spots appeared but remained approximately constant at ∼4,000 km s^{-1} (Ng et al. 2008).

The radio image has remained brighter on the east side (Ng et al. 2013), unlike the optical and X-ray images, which have become brighter on the west (**Figure 9**). The radio emission is evidently synchrotron radiation. It has a power-law spectrum (**Figure 5**), $S_\nu \propto \nu^{-\alpha}$, where the overall spectral index has evolved from $\alpha = 0.91$ at day 1,517 to $\alpha = 0.73$ at day 9,280.

The power-law spectrum of synchrotron radiation is believed to be the result of diffusive acceleration of relativistic electrons across a shock. According to the simplest version of this theory (e.g., Jones & Ellison 1991), the synchrotron spectral index is related to the shock compression ratio, σ, by $\alpha = 3/[2(\sigma - 1)]$. For a high Mach number shock such as the SN blast wave, $\sigma = 4$; hence $\alpha = 0.5$. The fact that the observed spectral index is steeper than this requires some modification of this theory. The situation is still unclear.

One possible explanation is that the shock compression ratio, σ, is less than 4. This might be the case if the electrons are accelerated primarily by the reflected shocks responsible for the hard X-ray emission. (For example, a plane-parallel shock from a blast wave reflected off a dense obstacle will have $M = 5^{1/2}$ and $\sigma = 2.5$; hence $\alpha = 1$.) Alternatively, the blast wave may be cushioned by a magnetic field. Another possibility (Kirk et al. 1996) is that the electrons undergo sub-diffusion in a turbulent magnetic field, in which case $\alpha = 9/[4(\sigma - 1)]$, which implies $\alpha = 0.75$ for $\sigma = 4$.

Clearly, the relativistic electrons in SN 1987A are accelerated in a different environment from that responsible for the optical and X-ray emission. One might conjecture that the injection of relativistic electrons has greater efficiency in a low-density environment than in the higher-density environment favored by the optical and X-ray emission. The brighter emission on the eastern lobe may be the result of a smaller fraction of injected particles than on the west.

The spectral analysis of ATCA and ALMA images from 7 mm to 870 μm shows $0.1 \lesssim \alpha \lesssim 0.4$ across the western regions of the remnant (Zanardo et al. 2014), which might be attributed to

particle flux injection by a possible pulsar (Gaensler & Slane 2006). This interpretation must be regarded as tentative given the contribution by thermal emission from cold dust in this band.

Potter et al. (2014) have developed an ambitious model to account for the evolution and morphology of the nonthermal emission from SN 1987A. The model consists of a hydrodynamic simulation of the SN explosion encountering a circumstellar environment similar to that proposed by Chevalier & Dwarkadas (1995). By incorporating semianalytic recipes for diffusive shock acceleration and magnetic field amplification into the hydrodynamic solutions and choosing parameters for the pre-SN environment, the authors are able to produce models that fit the evolution of the radio image reasonably well. An asymmetric SN explosion is required to account for the east-west asymmetry of the radio image. The model does not account for the evolution of the spectral index, however.

4.6. Very-High-Energy Gamma Rays

Based on ATCA radio observations, Berezhko et al. (2011) and Dwarkadas (2013) have predicted the TeV gamma rays resulting from the π^0 decay, which is produced by the interaction of the cosmic rays at the shocks with the protons in the circumstellar medium. Depending on the assumptions about the circumstellar medium properties, the expected flux was $\sim 2.5 \times 10^{-13}$ photons cm^{-2} s^{-1} (Berezhko et al. 2011) and $\sim 8 \times 10^{-14}$ photons cm^{-2} s^{-1} (Dwarkadas 2013).

The region around SN 1987A has recently been observed with the High Energy Stereoscopic System (HESS) gamma-ray telescope by Abramowski et al. (2015). While they find emission from nearby pulsar wind nebulae, young SN remnants, and stellar wind bubbles, SN 1987A only yielded an upper limit of $< 5 \times 10^{-14}$ photons cm^{-2} s^{-1} above 1 TeV, which is lower than the above predictions. There are, however, a number of uncertainties in the latter, in particular the proton injection rate, the nonthermal proton-to-electron ratio, the magnetic field, and the geometry and parameters of the shocks. Nevertheless, this shows that these observations in combination with the radio and hard X-ray observations can put interesting constraints on the efficiency of cosmic-ray acceleration. For SN 1987A, Abramowski et al. (2015) estimate that less than 1% of the explosion energy is in cosmic rays.

Recently, Berezhko et al. (2015) have revised their model to better comply with the observed structure and parameters of the circumstellar medium. In particular, the mass of the ER was decreased by an order of magnitude. With this change, the model flux decreased to close to the upper limit observed using the HESS.

5. HOW UNIQUE WAS SN 1987A?

The discovery that the progenitor of SN 1987A was a BSG rather than an RSG came as a big surprise. Since then, several cases of SNe with similar light curves and luminosities have been discovered.

Some 18 SNe have been identified with light curves similar to SN 1987A (Kleiser et al. 2011, Pastorello et al. 2012, Taddia et al. 2012, Arcavi et al. 2012, González-Gaitán et al. 2015). Because of the limited sample and their intrinsic faintness, the rate of these events is highly uncertain. Pastorello et al. (2012) estimate a rate of 1–3% of all core-collapse SNe to be photometrically similar to SN 1987A; this is similar to the estimate by Kleiser et al. (2011). Likewise, I. Shivvers (private communication) finds two SNe with light curves resembling SN 1987A among 135 core-collapse SNe in a volume-limited sample assembled from the Lick Observatory Supernova Search (Li et al. 2011).

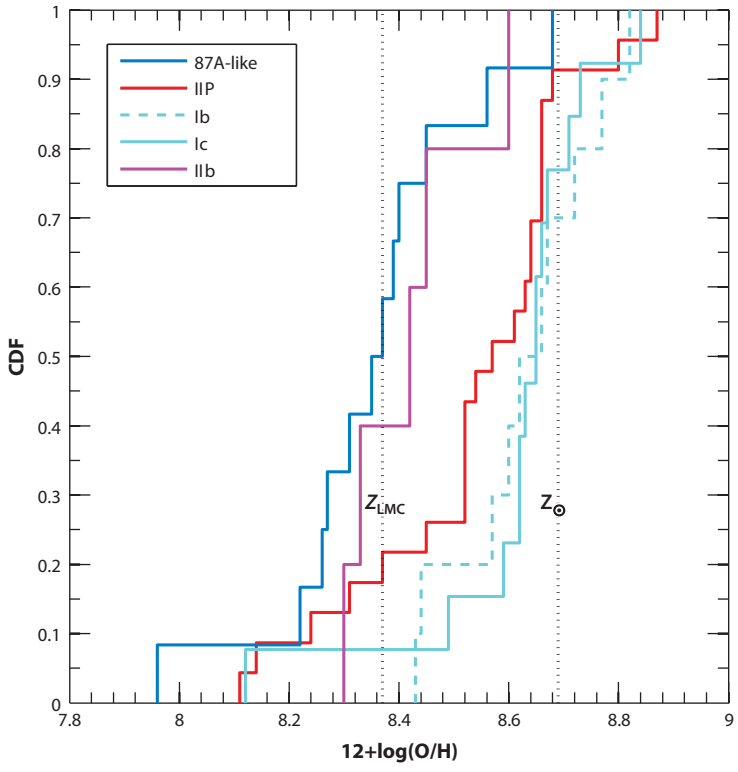

Figure 16

A cumulative distribution of the metallicity of the environment of Type II SNe with blue supergiant progenitors compared with distributions of Type IIP, Ib, and Ic SNe (Taddia et al. 2013). Abbreviations: CDF, Chandra Deep Field; LMC, Large Magellanic Cloud.

An important clue to the nature of the BSG progenitor may be the metallicity of the host environment. Early models showed that low metallicity indeed could lead to a BSG progenitor (Arnett et al. 1989). A recent study of SNe with light curves indicating a BSG progenitor by Taddia et al. (2013) shows that most of these occur in low-metallicity environments, such as low-luminosity galaxies, or at large distances from the nuclei of luminous hosts. (There are also cases with near-solar metallicity.) As shown in **Figure 16**, the metallicities are clearly different from those of the Type IIP SNe but similar to those of the Type IIb SNe.

There are several stars in our galaxy that are known to have ring systems resembling SN 1987A. The best-studied systems are Sher-25, HD168625, and SBW1 (Brandner et al. 1997, Nota et al. 1996, Smith 2007, Smith et al. 2013). All three have ERs with similar dimensions to that of SN 1987A. For SBW1 an hourglass structure emanating from the ring is seen, which may resemble the one that may be present in SN 1987A (Smith et al. 2013; see also **Figure 17**). The dust emission seen in the interior of the ring would be evaporated by the flash of extreme UV and soft X-rays at the time of the shock breakout (Fischera et al. 2002b).

HD168625 is a luminous blue variable with a ring system that closely resembles that of SN 1987A, including both an ER and two polar rings. The expansion velocities of the rings of these

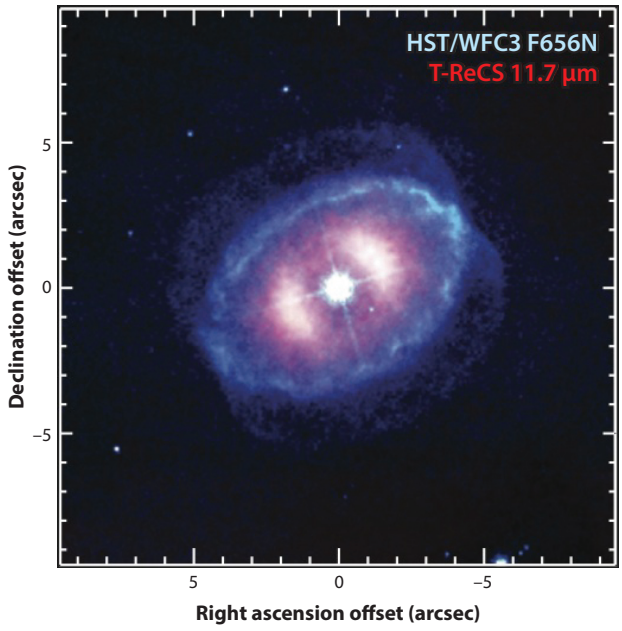

Figure 17

A composite image of the HST/WFC3 Hα image (*blue/green*), and the Gemini South T-ReCS 11.7-μm image (*red/orange*) of SBW1 (Smith et al. 2013). Note the hourglass structure in Hα above and below the ring and the dust emission from the interior.

three objects are $\sim$20 km s^{-1}, which is twice as high as for the inner ring of SN 1987A but similar to that for the outer rings.

In the case of Sher-25 the star has a luminosity considerably greater ($\log L = 5.9 \pm 0.2$ L$_\odot$, corresponding to a $\sim$60-M$_\odot$ zero-age main-sequence star) than Sanduleak $-69°$ 202 (which has $\log L = 5.1$ L$_\odot$). HD168625 has a variable luminosity of $\log L = 5.0 - 5.4$ L$_\odot$ (Nota et al. 1996). SBW1 is only somewhat more luminous than the progenitor of SN 1987A, with spectral types B 1.5Iab and B 3Ib, respectively, and may therefore in this respect be the star most similar to the SN 1987A progenitor.

Neither of these cases shows the large N/O ratio expected for a progenitor that has gone through an RSG phase. Lamers et al. (2001) find that RSGs should have surface abundances in the range of N/C = 6–30 and N/O = 3–20, whereas Sher-25 has N/O = 0.36; the others also have moderate N enrichments (Smartt et al. 2002, Smith et al. 2013). For SN 1987A, modeling of the IUE observations gives N/C = 5.0 ± 2.0 and N/O = 1.1 ± 0.4 (Lundqvist & Fransson 1996). Based on the low N enrichment, circumstellar structure, and other reasons, Smith (2007) has argued that the progenitor of SN 1987A may have been a low-luminosity luminous blue variable rather than a star that has passed the RSG phase.

Finally, we remark that though some properties, in particular the BSG progenitor and the circumstellar medium, are unique to this class of SNe, other aspects are typical for core-collapse SNe. This includes most of the core properties, like the neutrino burst, radioactivity and general nucleosynthesis, hydrodynamics, and dust formation. SN 1987A therefore still stands out as the most important object for understanding the physics of a core-collapse SN.

FUTURE ISSUES

We have learned more about SNe from SN 1987A than from any other SN, but we still have much to learn. Here are a few of the outstanding questions.

1. **Do we understand the explosion mechanism?** From observations of ions and molecules, we have well determined masses of the most abundant isotopes, good estimates of the masses, and some information on morphology of the most abundant elements in the ejecta. Much of this has been obtained thanks to new instruments and telescopes that have become available during the past decade.

   On the theoretical side there has been much progress in incorporating both more realistic physics and more powerful computing resources. Still, there is a lack of models that can be directly compared with the observations. Most explosion models are only calculated out to a few seconds, and the connection between the structure and nucleosynthesis at this epoch to what is observed when the core has become transparent is not well understood. Some steps in this direction have been taken (e.g., Utrobin et al. 2015, Wongwathanarat et al. 2015), but these are exceptions rather than a rule. A major uncertainty in the theoretical simulations stems from the distribution of products of nucleosynthesis prior to the explosion, which may be scrambled by violent convection in the late stages of pre-SN burning.

2. **How are the newly formed elements distributed throughout the SN debris?** We can be confident that we will make substantial progress in unraveling its mysteries, thanks in part to the evolution of the SN itself and also in large part to the dramatic advances in astronomical instrumentation.

   We have learned that most of the nucleosynthesis products are confined within a sphere expanding with a velocity of $\approx$1,500 km s^{-1} and are mixed macroscopically but not microscopically. With the ALMA, we have seen that CO and SiO have different distributions within this volume. In the next few years, we will be able to map the 3D distribution of CO and SiO with angular resolution at an order of magnitude better than heretofore.

   SINFONI gives a complementary view of the inner ejecta, which reflects the atomic constituent of the processed material. It is important to note that while the rotational transitions in the submillimeter range are excited by thermal collisions, the NIR lines are excited by the nonthermal excitations from the ^{44}Ti decay. Further, the submillimeter lines are unaffected by the dust. The NIR emission may still be affected by dust absorption and may be compared with the submillimeter emission observed by the ALMA to provide a view of the 3D dust distribution.

   In the next decade, the Giant Magellan Telescope and the European Extremely Large Telescope, with their enormous collecting areas and superior resolutions, will provide an even better 3D view of the ejecta at a time when the X-ray illumination from the ring interaction may reach the inner parts of the core. The *James Webb Space Telescope* will enable us to search for the MIR H_2 28-μm, [FeII] 26-μm, and FeI 24-μm lines with better resolution and sensitivity.

   We also know, from the early emergence of X-rays and gamma rays, as well as the wings of the [FeII] lines (Haas et al. 1990, Spyromilio et al. 1990), that some of the newly formed elements extend beyond the 1,500 km s^{-1} sphere (McCray 1993). As the debris continues to expand, the X-rays from the impact will penetrate deeper into the debris, eventually causing the debris to glow with optical/IR spectra characteristic of these elements. At

some uncertain time in the next few decades, the reverse shock will encounter newly formed elements, particularly the iron bubbles (Li et al. 1993), and deform rapidly, as illustrated in simulations by Blondin et al. (2001). Such an event will be accompanied by a rapid change in the X-ray spectrum of the shocked gas.

3. **What is the history of mass ejection by the progenitor?** The history of mass loss from the progenitor is imprinted on the distribution and kinematics of circumstellar matter. The mass of the visible ER inferred from observations, $M_i \sim 0.06\ M_\odot$ (Lundqvist & Fransson 1996, Mattila et al. 2010), is probably limited by the total number of ionizing photons from the initial flash of the SN. The recent appearance of new hot spots is evidence that we are now beginning to see heretofore invisible matter beyond the ER. Such matter will continue to brighten, steadily as it is ionized by X-rays from the shocked gas and more suddenly as the blast wave overtakes it. Moreover, the evolution of the remnant of SN 1987A will be determined by its distribution. Up to now, we can see that only a small fraction of the kinetic energy of the ejecta has been converted to radiation through the impact with this matter. This fraction will approach unity only when the blast wave has overtaken a mass comparable with that of the ejecta. As we have seen, most of this conversion is presently taking place where the blast wave is striking the ER. We do not know how much mass lies beyond the visible ring. If it is substantial (i.e., $\sim 1\ M_\odot$), the reverse shock will continue to dig into the ejecta in the equatorial plane and will reach the inner ($V \lesssim 2{,}000$ km s^{-1}) nucleosynthesis products by $t \sim 1$ century. At roughly the same time, the blast wave will strike the outer loops and cause them to brighten. However, if the blast wave has overtaken most of the ER, the pressure driving the reverse shock will diminish, and it will take longer for the reverse shock to reach the nucleosynthesis products. In any case, it seems likely that the morphology of the remnant of SN 1987A will be determined by the history of mass loss by the progenitor for several centuries.

   Deep imaging and spectroscopy with the HST, ground-based optical/IR telescopes, *Chandra*, and eventually the *James Webb Space Telescope* will give us the clues we need to reconstruct this history. Comparisons with other SN 1987A-like SNe and progenitor systems may give additional insight into the progenitor evolution.

4. **How are relativistic electrons and cosmic rays accelerated in SN shocks?** The nonthermal (millimeter to centimeter) radiation from SN 1987A gives us our first chance to observe acceleration of relativistic electrons by SN shocks in real time. We have already seen that the morphology and evolution of this radiation differ substantially from those of the optical and X-ray emission from the shocked gas. With the ALMA, we will soon be able to obtain images of the nonthermal radiation and its polarization with angular resolution better than 0.1 arcsec. Optical images and spectra of comparable resolution from the HST will enable us to characterize the physical conditions in the shocks where the relativistic electrons are accelerated. On a longer timescale the Cherenkov Telescope Array will improve the sensitivity of the HESS for TeV gamma rays by an order of magnitude, which should challenge the predictions for cosmic ray production in SN 1987A (Section 4.6).

5. **What is the compact object?** The initial burst of neutrinos from SN 1987A is compelling evidence that a compact object was formed during its core collapse (Arnett et al. 1989). The object is most likely a neutron star, but it is possible that continued infall triggered a further collapse to a black hole.

Despite intensive efforts, using the most sensitive available instruments spanning the entire electromagnetic spectrum, astronomers have been unable to detect any signal from the compact object since the neutrino burst. Little has changed since McCray (2007) reviewed the situation. The upper limit to the luminosity of the compact object is a few tens of $L_\odot$. Graves et al. (2005) find an upper limit of only $\sim$1.3 $L_\odot$ between 2900–9650 Å. The dust we know is present in the core may, however, convert any emission in the UV, optical, and NIR ranges from a pulsar wind nebula to the FIR range.

The expectation that we might find a bright compact object at the center of SN 1987A has been dampened somewhat by the observations that several SN remnants, notably Cas A, have compact sources with an X-ray luminosity less than a few $L_\odot$ and no radio emission (De Luca 2008). Evidently, these sources are cooling neutron stars with very weak magnetic fields. If SN 1987A contained such a neutron star, it would not have been detected by current methods.

Our best hope to detect the compact object is to image SN 1987A with higher angular resolution than heretofore. With the ALMA it will soon be possible to search for a compact flat spectrum radio source near the center of the explosion debris or a compact component to the thermal dust emission.

DISCLOSURE STATEMENT

The authors are not aware of any affiliations, memberships, funding, or financial holdings that might be perceived as affecting the objectivity of this review.

ACKNOWLEDGMENTS

We thank the following people for advice and assistance with this review: Adam Burrows, David Burrows, Pete Challis, Roger Chevalier, Eli Dwek, Kari Frank, Anders Jerkstrand, Patrick Kelly, Josefin Larsson, Peter Lundqvist, Mikako Matsuura, Katia Migotto, Francesco Taddia, Stan Woosley, and Giovanna Zanardo. The research of C.F. is supported by the Swedish Research Council and Swedish National Space Board.

LITERATURE CITED

Abramowski A, Aharonian F, Ait Benkhali F, et al. 2015. *Science* 347:406–12
Arcavi I, Gal-Yam A, Cenko SB, et al. 2012. *Ap. J. Lett.* 756:L30
Arnett WD, Bahcall JN, Kirshner RP, Woosley SE. 1989. *Annu. Rev. Astron. Astrophys.* 27:629–700
Axelrod TS. 1980. *Late time optical spectra from the Ni-56 model for type 1 supernovae*. PhD thesis, Univ. Calif., Santa Cruz
Ball L, Crawford DF, Hunstead RW, Klamer I, McIntyre VJ. 2001. *Ap. J.* 549:599–607
Berezhko EG, Ksenofontov LT, Völk HJ. 2011. *Ap. J.* 732:58
Berezhko EG, Ksenofontov LT, Völk HJ. 2015. *Ap. J.* 810:63
Blinnikov S, Lundqvist P, Bartunov O, Nomoto K, Iwamoto K. 2000. *Ap. J.* 532:1132–49
Blondin JM, Borkowski KJ, Reynolds SP. 2001. *Ap. J.* 557:782–91
Boggs SE, Harrison FA, Miyasaka H, et al. 2015. *Science* 348:670–71
Borkowski KJ, Blondin JM, McCray R. 1997. *Ap. J. Lett.* 476:L31–34
Bouchet P, Danziger J. 2014. In *Supernova Environmental Impacts, Proc. IAU Symp. 296*, ed. A Ray, RA McCray, 9:9–14. Cambridge, UK: Cambridge Univ. Press
Bouchet P, Dwek E, Danziger J, et al. 2006. *Ap. J.* 650:212–27

Brandner W, Chu YH, Eisenhauer F, Grebel EK, Points SD. 1997. *Ap. J. Lett.* 489:L153–56
Burrows A. 2013. *Rev. Mod. Phys.* 85:245–61
Burrows DN, Michael E, Hwang U, et al. 2000. *Ap. J. Lett.* 543:L149–52
Chevalier RA, Dwarkadas VV. 1995. *Ap. J. Lett.* 452:L45–48
Chita SM, Langer N, van Marle AJ, García-Segura G, Heger A. 2008. *Astron. Astrophys.* 488:L37–41
Chugai NN, Chevalier RA, Kirshner RP, Challis PM. 1997. *Ap. J.* 483:925–40
Couch SM, Chatzopoulos E, Arnett WD, Timmes FX. 2015. *Ap. J. Lett.* 808:L21
Crotts APS, Heathcote SR. 2000. *Ap. J.* 528:426–35
Culhane M, McCray R. 1995. *Ap. J.* 455:335–41
de Kool M, Li H, McCray R. 1998. *Ap. J.* 503:857–76
De Luca A. 2008. In *40 Years of Pulsars: Millisecond Pulsars, Magnetars and More*, ed. C Bassa, Z Wang, A Cumming, VM Kaspi. *AIP Conf. Ser.* 983:311–19. Melville, NY: AIP
Dessart L, Hillier DJ. 2010. *MNRAS* 405:2141–60
Dewey D, Zhekov SA, McCray R, Canizares CR. 2008. *Ap. J. Lett.* 676:L131–34
Dwarkadas VV. 2013. *MNRAS* 434:3368–77
Dwek E, Arendt RG. 2015. *Ap. J.* 10:75–85
Dwek E, Arendt RG, Bouchet P, et al. 2008. *Ap. J.* 676:1029–39
Dwek E, Arendt RG, Bouchet P, et al. 2010. *Ap. J.* 722:425–34
Ensman L, Burrows A. 1992. *Ap. J.* 393:742–55
Fischera J, Tuffs RJ, Völk HJ. 2002a. *Astron. Astrophys.* 386:517–30
Fischera J, Tuffs RJ, Völk HJ. 2002b. *Astron. Astrophys.* 395:189–200
France K, McCray R, Fransson C, et al. 2015. *Ap. J. Lett.* 801:L16
France K, McCray R, Heng K, et al. 2010. *Science* 329:1624–27
France K, McCray R, Penton SV, et al. 2011. *Ap. J.* 743:186
Frank KA, Dwek E, McCray R, Park S, Zhekov SA, Burrows DN. 2016. *Ap. J.* In press
Fransson C, Cassatella A, Gilmozzi R, et al. 1989. *Ap. J.* 336:429–41
Fransson C, Kozma C. 1993. *Ap. J. Lett.* 408:L25–28
Fransson C, Kozma C. 2002. *New Astron. Rev.* 46:487–92
Fransson C, Larsson J, Migotto K, et al. 2015. *Ap. J. Lett.* 806:L19
Fransson C, Larsson J, Spyromilio J, et al. 2013. *Ap. J.* 768:88–110
Fransson C, Larsson J, Spyromilio J, Leibundgut B, McCray R, Jerkstrand A. 2016. *Ap. J. Lett.* 821:L5
Gaensler BM, Slane P. 2006. *Annu. Rev. Astron. Astrophys.* 44:17–47
González-Gaitán S, Tominaga N, Molina J, et al. 2015. *MNRAS* 451:2212–29
Gould A, Uza O. 1998. *Ap. J.* 494:118–24
Graves GJM, Challis PM, Chevalier RA, et al. 2005. *Ap. J.* 629:944–59
Grebenev SA, Lutovinov AA, Tsygankov SS, Winkler C. 2012. *Nature* 490:373–75
Gröningsson P, Fransson C, Leibundgut B, et al. 2008. *Astron. Astrophys.* 492:481–91
Gröningsson P, Fransson C, Lundqvist P, et al. 2006. *Astron. Astrophys.* 456:581–89
Haas MR, Erickson EF, Lord SD, et al. 1990. *Ap. J.* 360:257–66
Hammer NJ, Janka HT, Müller E. 2010. *Ap. J.* 714:1371–85
Hanuschik RW, Thimm GJ. 1990. *Astron. Astrophys.* 231:77–84
Hashimoto M, Nomoto K, Shigeyama T. 1989. *Astron. Astrophys.* 210:L5–8
Hasinger G, Aschenbach B, Truemper J. 1996. *Astron. Astrophys.* 312:L9–12
Helder EA, Broos PS, Dewey D, et al. 2013. *Ap. J.* 764:11
Heng K, McCray R, Zhekov SA, et al. 2006. *Ap. J.* 644:959–70
Herant M, Benz W. 1991. *Ap. J. Lett.* 370:L81–84
Herant M, Benz W, Colgate S. 1992. *Ap. J.* 395:642–53
Herant M, Benz W, Hix WR, Fryer CL, Colgate SA. 1994. *Ap. J.* 435:339–61
Indebetouw R, Matsuura M, Dwek E, et al. 2014. *Ap. J. Lett.* 782:L2
Jäger C, Dorschner J, Mutschke H, Posch T, Henning T. 2003. *Astron. Astrophys.* 408:193–204
Janka HT. 2012. *Annu. Rev. Nucl. Part. Sci.* 62:407–51
Janka HT, Hanke F, Hüdepohl L, et al. 2012. *Prog. Theor. Exp. Phys.* 2012:01A309
Jerkstrand A, Fransson C, Kozma C. 2011. *Astron. Astrophys.* 530:A45

Jones FC, Ellison DC. 1991. *Space Sci. Rev.* 58:259–346
Kamenetzky J, McCray R, Indebetouw R, et al. 2013. *Ap. J. Lett.* 773:L34
Kirk JG, Duffy P, Gallant YA. 1996. *Astron. Astrophys.* 314:1010–16
Kjær K, Leibundgut B, Fransson C, Jerkstrand A, Spyromilio J. 2010. *Astron. Astrophys.* 517:A51
Kleiser IKW, Poznanski D, Kasen D, et al. 2011. *MNRAS* 415:372–82
Kozma C, Fransson C. 1992. *Ap. J.* 390:602–21
Kozma C, Fransson C. 1998a. *Ap. J.* 496:946–66
Kozma C, Fransson C. 1998b. *Ap. J.* 497:431–57
Lakićević M, van Loon JT, Stanke T, De Breuck C, Patat F. 2012a. *Astron. Astrophys.* 541:L1
Lakićević M, Zanardo G, van Loon JT, et al. 2012b. *Astron. Astrophys.* 541:L2
Lamers HJGLM, Nota A, Panagia N, Smith LJ, Langer N. 2001. *Ap. J.* 551:764–80
Larsson J, Fransson C, Kjaer K, et al. 2013. *Ap. J.* 768:89
Larsson J, Fransson C, Östlin G, et al. 2011. *Nature* 474:484–86
Lawrence SS, Sugerman BE, Bouchet P, et al. 2000. *Ap. J. Lett.* 537:L123–26
Li H, McCray R. 1993. *Ap. J.* 405:730–37
Li H, McCray R. 1996. *Ap. J.* 456:370–83
Li H, McCray R, Sunyaev RA. 1993. *Ap. J.* 419:824–36
Li W, Leaman J, Chornock R, et al. 2011. *MNRAS* 412:1441–72
Liu W, Dalgarno A. 1994. *Ap. J.* 428:769–76
Liu W, Dalgarno A. 1995. *Ap. J.* 454:472–79
Liu W, Dalgarno A, Lepp S. 1992. *Ap. J.* 396:679–85
Lundqvist P, Fransson C. 1991. *Ap. J.* 380:575–92
Lundqvist P, Fransson C. 1996. *Ap. J.* 464:924–42
Lundqvist P, Sollerman J, Kozma C, et al. 1999. *Astron. Astrophys.* 347:500–7
Luo D, McCray R, Slavin J. 1994. *Ap. J.* 430:264–76
Mathis JS, Rumpl W, Nordsieck KH. 1977. *Ap. J.* 217:425–33
Manchester RN, Gaensler BM, Wheaton VC, et al. 2002. *Publ. Astron. Soc. Aust.* 19:207–21
Matsuura M, Dwek E, Barlow MJ, et al. 2015. *Ap. J.* 800:50
Matsuura M, Dwek E, Meixner M, et al. 2011. *Science* 333:1258–61
Mattila S, Lundqvist P, Gröningsson P, et al. 2010. *Ap. J.* 717:1140–56
McCray R. 1993. *Annu. Rev. Astron. Astrophys.* 31:175–216
McCray R. 2007. In *Supernova 1987A: 20 Years After: Supernovae and Gamma-Ray Bursters*, ed. S Immler, K Weiler, R McCray. *AIP Conf. Ser.* 937:3–14. Melville, NY: AIP
Michael E, McCray R, Chevalier R, et al. 2003. *Ap. J.* 593:809–30
Michael E, McCray R, Pun CSJ, et al. 1998. *Ap. J. Lett.* 509:L117–20
Michael E, Zhekov S, McCray R, et al. 2002. *Ap. J.* 574:166–78
Morris T, Podsiadlowski P. 2007. *Science* 315:1103–5
Morris T, Podsiadlowski P. 2009. *MNRAS* 399:515–38
Ng CY, Gaensler BM, Staveley-Smith L, et al. 2008. *Ap. J.* 684:481–97
Ng CY, Zanardo G, Potter TM, et al. 2013. *Ap. J.* 777:131
Nisenson P, Papaliolios C, Karovska M, Noyes R. 1987. *Ap. J. Lett.* 320:L15–18
Nota A, Pasquali A, Clampin M, et al. 1996. *Ap. J.* 473:946–62
O'Dell CR, Handron KD. 1996. *Astron. J.* 111:1630–779
Orlando S, Miceli M, Pumo ML, Bocchino F. 2015. *Ap. J.* 810:168–84
Panagia N, Gilmozzi R, Macchetto F, Adorf HM, Kirshner RP. 1991. *Ap. J. Lett.* 380:L23–26
Papaliolios C, Karovska M, Koechlin L, et al. 1989. *Nature* 338:565–66
Pastorello A, Pumo ML, Navasardyan H, et al. 2012. *Astron. Astrophys.* 537:A141
Pinto PA, Woosley SE, Ensman LM. 1988. *Ap. J. Lett.* 331:L101–4
Potter TM, Staveley-Smith L, Reville B, et al. 2014. *Ap. J.* 794:174
Pun CSJ, Michael E, Zhekov SA, et al. 2002. *Ap. J.* 572:906–31
Racusin JL, Park S, Zhekov S, et al. 2009. *Ap. J.* 703:1752–59
Sana H, de Mink SE, de Koter A, et al. 2013. In *370 Years of Astronomy in Utrecht*, ed. G Pugliese, A de Koter, M Wijburg. *ASP Conf. Ser.* 470:141–45. San Francisco: ASP

Sapir N, Halbertal D. 2014. *Ap. J.* 796:145
Sapir N, Katz B, Waxman E. 2013. *Ap. J.* 774:79
Sarangi A, Cherchneff I. 2015. *Astron. Astrophys.* 575:A95
Seitenzahl IR, Taubenberger S, Sim SA. 2009. *MNRAS* 400:531–35
Sinnott B, Welch DL, Rest A, Sutherland PG, Bergmann M. 2013. *Ap. J.* 767:45
Smartt SJ, Lennon DJ, Kudritzki RP, et al. 2002. *Astron. Astrophys.* 391:979–91
Smith N. 2007. *Astron. J.* 133:1034–40
Smith N, Arnett WD, Bally J, Ginsburg A, Filippenko AV. 2013. *MNRAS* 429:1324–41
Smith N, Zhekov SA, Heng K, et al. 2005. *Ap. J. Lett.* 635:L41–44
Soker N. 1998. *Ap. J.* 496:833–41
Sonneborn G, Fransson C, Lundqvist P, et al. 1997. *Ap. J.* 477:848–64
Sonneborn G, Pun CSJ, Kimble RA, et al. 1998. *Ap. J. Lett.* 492:L139–42
Spyromilio J, Meikle WPS, Allen DA. 1990. *MNRAS* 242:669–73
Staveley-Smith L, Potter TM, Zanardo G, Gaensler BM, Ng CY. 2014. In *Supernova Environmental Impacts*, *Proc. IAU Symp. 296*, ed. A Ray, RA McCray. 9:15–22. Cambridge, UK: Cambridge Univ. Press
Sturm R, Haberl F, Aschenbach B, Hasinger G. 2010. *Astron. Astrophys.* 515:A5
Sukhbold T, Ertl T, Woosley SE, Brown JM, Janka HT. 2016. *Ap. J.* 821:38
Sugerman BEK, Crotts APS, Kunkel WE, Heathcote SR, Lawrence SS. 2005. *Ap. J. Suppl.* 159:60–99
Taddia F, Sollerman J, Razza A, et al. 2013. *Astron. Astrophys.* 558:A143
Taddia F, Stritzinger MD, Sollerman J, et al. 2012. *Astron. Astrophys.* 537:A140
Tanaka T, Washimi H. 2002. *Science* 296:321–22
Turtle AJ, Campbell-Wilson D, Manchester RN, Staveley-Smith L, Kesteven MJ. 1990. *IAU Circ.* 5086:2
Tziamtzis A, Lundqvist P, Gröningsson P, Nasoudi-Shoar S. 2011. *Astron. Astrophys.* 527:A35
Utrobin V, Wongwathanarat A, Janka HT, Müller E. 2015. *Astron. Astrophys.* 581:40–58
Utrobin VP, Chugai NN. 2005. *Astron. Astrophys.* 441:271–81
Wang L, Wheeler JC, Höflich P, et al. 2002. *Ap. J.* 579:671–77
Wesson R, Barlow MJ, Matsuura M, Ercolano B. 2015. *MNRAS* 446:2089–101
Wongwathanarat A, Müller E, Janka HT. 2015. *Astron. Astrophys.* 577:A48
Wooden DH, Rank DM, Bregman JD, et al. 1993. *Ap. J. Suppl.* 88:477–507
Woosley SE. 1988. *Ap. J.* 330:218–53
Woosley SE, Hartmann D, Pinto PA. 1989. *Ap. J.* 346:395–404
Xu Y, McCray R. 1991. *Ap. J.* 375:190–201
Zanardo G, Staveley-Smith L, Ball L, et al. 2010. *Ap. J.* 710:1515–29
Zanardo G, Staveley-Smith L, Indebetouw R, et al. 2014. *Ap. J.* 796:82
Zhekov SA, McCray R, Borkowski KJ, Burrows DN, Park S. 2005. *Ap. J. Lett.* 628:L127–30
Zhekov SA, McCray R, Borkowski KJ, Burrows DN, Park S. 2006. *Ap. J.* 645:293–302